The Astrophysical Journal, 947:15 (22pp), 2023 April 10 https://doi.org/10.3847/1538-4357/acb20e

Cooling Rates of Chondrules after Lightning Discharge in Solid-rich Environments

Hiroaki Kaneko, Kento Sato, Chihiro Ikeda, and Taishi Nakamoto
Department of Earth and Planetary Sciences, Tokyo Institute of Technology, 2-12-1 Ookayama, Meguro-ku, Tokyo 152-8550 Japan; kaneko.h.aq@m.titech.ac.jp
Received 2022 May 7; revised 2022 November 5; accepted 2023 January 9; published 2023 April 12

Abstract

Among the several candidate models for chondrule formation, the lighting model has been recognized to be less likely than the other two major models, shock-wave heating and planetesimal collision. It might be because we have believed that the lightning model predicts cooling rates of chondrules that are too fast to reproduce their textures with the assumption that the discharge channels must be optically thin. However, the previous works revealed that the buildup of a strong electric field to generate the lightning in protoplanetary disks requires the enhancement of the solid density. Moreover, some properties of chondrules indicate their formation in environments with such a high solid density. Therefore, the discharge channels may be optically thick, and the lightning model can potentially predict the proper cooling rates of chondrules. In this study, we reinvestigate the cooling rates of chondrules produced by the lightning in the solid-rich environments considering the radiative transfer and the expansion of the hot channel. Chondrules must interact dynamically with the surrounding gas and dust via the drag force. We consider two limiting cases for the dynamics of chondrules: the drag force is ignored in the first case, and chondrules are completely coupled with their surroundings in the second case. In both cases, the lightning model predicts the proper cooling rates of chondrules under the optically thick conditions with high solid enhancement. Therefore, the lightning model is worth further investigation to judge its reliability as the source of chondrule formation.

Unified Astronomy Thesaurus concepts: Chondrules (229); Chondrites (228); Hydrodynamics (1963); Radiative transfer (1335)

1. Introduction

The birth of planets proceeds in the gas disks rotating around central stars, and such gas disks are called protoplanetary disks. Both theoretical and observational understandings of planet formation and the evolution of protoplanetary disks have been progressing thanks to the development of models and observational instruments. Today, we can observe the evolving protoplanetary disks and exoplanets beyond our solar system, and our attention is directed to the establishment of statistical explanations of these systems. However, our solar system is still an important target of planetary science. One of the reasons is that we can take in hand the precious clues to the processes of planet formation and the evolution of the protoplanetary disk (solar nebula) from the records in meteorites.

Chondrites occupy the majority of meteorites. The parent bodies of chondrites did not undergo internal differentiation; therefore, the primitive materials in the solar nebula are preserved in chondrites. Chondrites are mainly composed of four components: chondrules, matrix, refractory inclusions, and metals (e.g., Scott & Krot 2014). There is a long-standing mystery about the origins of chondrules (e.g., Desch et al. 2012; Connolly & Jones 2016). Chondrules are submillimeter- to millimeter-sized igneous spherules and might have experienced a molten phase and solidified during flash heating events in the solar nebula. They are abundant (up to 60–80 vol.% in ordinary chondrites) in all of the chondrite subgroups except CI chondrites, which might have suffered intense aqueous alteration in the parent bodies (e.g., Scott & Krot 2014). This common appearance of chondrules in chondrites indicates that they might have been ubiquitously distributed in the inner solar system, when the parent bodies of chondrites accreted. Therefore, uncovering the nature of the chondrule-forming events provides us invaluable insights into the physical and chemical environment and evolution of the solar nebula, so many measurements and experiments on chondrule compositions and textures have been conducted, and many models of chondrule-forming events have been suggested by a lot of works. However, we still do not have the conclusive answers regarding the origins of chondrules.

There are several candidate models for chondrule-forming events. Two major models, the shock-wave heating model (e.g., Iida et al. 2001; Ciesla & Hood 2002; Desch & Connolly 2002) and the planetesimal collision model (e.g., Asphaug et al. 2011; Johnson et al. 2015; Hasegawa et al. 2016), are favored by many authors. The shock-wave heating model includes some categories for the mechanisms of the shocks. In the bow shock model (e.g., Hood 1998; Weidenschilling et al. 1998; Ciesla et al. 2004; Morris et al. 2012; Boley et al. 2013; Mann et al. 2016; Mai et al. 2018; Nagasawa et al. 2019), the shock fronts are generated in front of the eccentric planetesimals (or embryos) perturbed by massive planets such as Jupiter due to the supersonic relative velocity between the circularly orbiting gas and the eccentric planetesimals. In the gravitational instability model (e.g., Hood & Horanyi 1991; Wood 1996; Boss & Durisen 2005), the spiral arms are excited in the self-gravitating disks, and the velocity difference between the spiral arms and nebula gas with the Keplerian orbit results in the generation of shock fronts. In any category of shock models, chondrule precursors crossing the shock fronts are gradually decelerated to the gas motion by the drag force and melted by drag heating, while the nebula gas crossing the shock fronts is quickly decelerated.

The planetesimal collision model is divided into two scenarios: low velocity (e.g., Asphaug et al. 2011) and high velocity (e.g., Johnson et al. 2015; Hasegawa et al. 2016; Wakita et al. 2017, 2021). Asphaug et al. (2011) suggested a scenario where the splash ejected from the planetesimals melting due to the energy input from the decay of ^{26}Al crystallizes to be chondrules. Johnson et al. (2015) suggested another scenario, where the jets are ejected from the solid planetesimals colliding at a high velocity exceeding $\sim$2.5 km s^{-1}, and chondrules are formed from these jets.

The reliable models of chondrule-forming events must be consistent with some constrains from the properties of chondrules. Specifically, the constraints on the thermal histories of chondrules are powerful tools to test the models (e.g., Desch et al. 2012). The experiments investigated the proper ranges of the heating and cooling rates of chondrules (see Desch et al. 2012, and references therein). Previous theoretical works tested the shock-wave heating (e.g., Desch & Connolly 2002; Ciesla et al. 2004; Morris et al. 2012) and planetesimal collision (e.g., Dullemond et al. 2014, 2016; Choksi et al. 2021) models in terms of the cooling rates of chondrules, and these models succeeded in predicting the cooling rates of $\sim 10^1$–10^3 K hr^{-1} at the subliquidus temperature expected from the experiments to reproduce the chondrule's textures (Desch et al. 2012), while the bow shock model might need some limitations (e.g., Boley et al. 2013; Mann et al. 2016).

However, there are several problems with these models. The shock model predicts collision velocities between two chondrules that are too fast to form compound chondrules, two or more chondrules fused together. The high-velocity collisions result in the breakup of chondrules instead of the fusion of the colliding chondrules (Jacquet & Thompson 2014). It is also difficult to explain the high solid density in the chondrule-forming environments, which is demanded from some properties of chondrules, such as the stabilization of the liquid phase, the lack of isotopic fractionation of volatiles, the retention of volatiles, and the redox states of the chondrule-forming environments in the context of the shock-wave heating model. While the collision model can predict a high enough solid density, the melting planetesimals in the low-velocity scenario by Asphaug et al. (2011) might differentiate, and the splash ejected from these bodies might have a nonchondritic composition, which is not true for chondrules (Lichtenberg et al. 2018). The solid planetesimals in the high-velocity (jet) scenario by Johnson et al. (2015) mitigate this problem, but the production rates of chondrules by this scenario are low. Just a few percent of the mass of the colliding planetesimals turns into chondrules (Johnson et al. 2015; Wakita et al. 2017, 2021). Though Johnson et al. (2015) and Hasegawa et al. (2016) confirmed that the cumulative mass of chondrules exceeding the present asteroid belt mass could be formed in the asteroid region in the jet scenario, it remains uncertain whether this efficiency and the amount of production of the chondrules are sufficient to explain the current occurrence of chondrules in chondrites. Moreover, chondrule-forming events might have prevailed to the outer disk region because fragments of chondrules were also discovered in the comet Wild2 (e.g., Nakamura et al. 2008). The collisional frequencies are lower in the outer disk region, so it is also uncertain whether the jet scenario can form chondrules beyond the asteroid region within the lifetime of the solar nebula.

The lightning model (e.g., Horányi et al. 1995; Desch & Cuzzi 2000; Muranushi 2010; Johansen & Okuzumi 2018) is another candidate for chondrule-forming events. Electrons in the gas medium are accelerated by the electric field before hitting the neutral molecules. Under a sufficiently strong electric field, the neutral–electron collisions lead to the ionization of the neutrals and a rapid increase in the electron density. It enhances the conductivity of the discharge current, and the energy stored in the electric field is liberated. The generation of lightning in protoplanetary disks does not easily happen everywhere; it requires very efficient charging and charge separation mechanisms because protoplanetary disks are weakly ionized, and the neutralizing currents prevent the buildup of the strong electric field (e.g., Desch & Cuzzi 2000; Muranushi 2010; Johansen & Okuzumi 2018). A lot of previous works on the lightning model focused on achieving the charging of the particles and overcoming the neutralizing currents to build the electric field. Desch & Cuzzi (2000) and Muranushi (2010) considered the collisional charging of the particles. Desch & Cuzzi (2000) suggested the buildup of the electric field by the concentration of the charged chondrule precursors into clumps by the concentration mechanism of the turbulent eddies. Muranushi (2010) added the regimes at the high solid density to the model of the equilibrium charge density distribution in protoplanetary disks and derived the analytical formulae of the critical solid density for the lightning to take place in protoplanetary disks with the parameters on the morphologies of the precursor aggregates of chondrules. Johansen & Okuzumi (2018) suggested the new charging and charge separation mechanism by the escape of positrons released from the decay of ^{26}Al in the dense midplane layers of protoplanetary disks or in the circumplanetesimal disks.

While the generation of lightning in protoplanetary disks is not necessarily impossible, the lightning model is often unfavored and outside of the spotlight. One of the reasons for it might be that the lightning model has been believed to predict cooling rates of chondrules that are too fast to reproduce their textures. A single isolated chondrule emits radiation escaping into space, and its temperature drops at the rate of $\sim 10^6$ K hr^{-1} during crystallization, which is orders of magnitude faster than the proper cooling rates of 10^1–10^3 K hr^{-1} reported from the experiments. Previous works (e.g., Horányi et al. 1995; Desch et al. 2012) assumed that the discharge channels are optically thin and that the cooling rates of chondrules inside the channels are like those of the isolated chondrule.

However, the buildup of the electric field in protoplanetary disks requires a high solid density to overcome the neutralizing currents. If the lightning happens in protoplanetary disks, the heated regions inside the discharge channels can be optically thick. In this case, the chondrules absorb the radiation emitted from the neighborhood chondrules, making the cooling rates of the chondrules much slower. Interestingly, Alexander et al. (2008) estimated that sodium retention in chondrules requires a solid density of $\sim 10^{-3}$–10^{-5} g cm^{-3}. The scenario where the lightning is generated in environments with such extremely high solid densities and produces chondrules at the cooling rates reported from the experiments cannot be ruled out.

In this paper, we reconsider the cooling rates of chondrules predicted by the lightning model. Johansen & Okuzumi (2018) showed that the cooling rates of chondrules produced by the lightning discharge really could be within the range of

10^1–10^3 K hr^{-1} in their simulations of the simplified radiative transfer. However, they did not consider the dynamics of the hot discharge channels. We solve the fluid dynamics of the hot solid-rich gas simultaneously with the radiative transfer and clarify how the dynamics of the discharge channels affects the formation of chondrules.

This paper is organized as follows. In Section 2, we introduce our model and basic equations. In Section 3, we explain the method to solve the equations introduced in Section 2. In Section 4, we show our calculation results on the evolution of the hot channels and the cooling rates of chondrules. In Section 5, we discuss the dynamics and cooling rates of chondrules from the analytical perspective, the environments suitable for chondrule formation via lightning, and compound chondrule formation. We also present the caveats of our model and the effects we do not consider in Section 5.

2. Model

We focus on the thermal histories of chondrules produced by lightning. We skip the issues of how to generate the lightning in protoplanetary disks. Our calculations start from a discharge channel filled with hot chondrules and gas produced by lightning. We approximate this channel as an infinitely long, uniform, axisymmetric cylindrical column. Based on terrestrial lightning, the width or radius of the channel $r_{\rm dis}$ can be scaled by the electron–neutral collision mean free path to nebula hydrogen molecules $\lambda_{\rm ne}$ and might be within the range of $10^3 \lesssim r_{\rm dis}/\lambda_{\rm ne} \lesssim 10^4$ (Horányi et al. 1995). The mean free path to hydrogen molecules is (Desch & Cuzzi 2000)

$$\lambda_{\rm ne} = 71\ {\rm cm}\left(\frac{\rho_{\rm H_2}}{10^{-10}\ {\rm g\ cm^{-3}}}\right)^{-1}, \tag{1}$$

and the channel radius is (Horányi et al. 1995)

$$r_{\rm dis} = 0.71\ {\rm km}\left(\frac{f_{\rm width}}{10^3}\right)\left(\frac{\rho_{\rm H_2}}{10^{-10}\ {\rm g\ cm^{-3}}}\right)^{-1}, \tag{2}$$

where $f_{\rm width}$ is the scaling factor.

We examine the cooling rates of chondrules inside the optically thick hot column. Chondrules cool down primarily due to their thermal radiation. However, the absorption of the radiation from the neighborhood chondrules and other particles slows down the cooling of the chondrules. As a result, the cooling of the chondrules is regulated by radiative diffusion in the optically thick column.

We assume that two populations of silicate particles exist: the first one is chondrules, and the second one is small dust grains. This assumption is partially motivated by scenarios where the size-dependent dynamics of the charged particles separate the charges and build up the electric field. Small dust grains might be produced by the fragmentation of larger particles such as chondrule precursors or the recondensation of silicate vapor evaporated from chondrules (see Subsection 5.3.3). These small dust grains might eventually compose the matrix in the final chondrite bodies.

The hot column expands due to its higher pressure than the outer ambient gas. This expansion was not taken into consideration in Johansen & Okuzumi (2018). The partial pressure of the vapor evaporated from the silicate particles must increase the total pressure.

Chondrules inside the expanding column dynamically interact with the surrounding gas and dust via the drag force to some degree. To clarify the impacts of the dynamics on the evolution of the hot column and the thermal histories of chondrules, we consider two limiting cases: completely decoupled and completely coupled. In the decoupled case, the drag force is neglected, so the chondrules do not move from their initial positions. On the other hand, in the coupled case, the chondrules and their surroundings are well coupled to each other via the drag force, and they share the same velocities.

Then, the following equations are what we solve:

$$\frac{\partial \rho}{\partial t} + \boldsymbol{\nabla}\cdot\rho\boldsymbol{v} = 0, \tag{3}$$

$$\begin{cases} \rho_{\rm c} = \rho_{\rm c,0} \quad \text{(decoupled)}, & \text{(4a)} \\ \dfrac{\rho_{\rm c}}{\rho_{\rm c,0}} = \dfrac{\rho}{\rho_0} \quad \text{(coupled)}, & \text{(4b)} \end{cases}$$

$$\begin{cases} \dfrac{\partial \rho\boldsymbol{v}}{\partial t} + \boldsymbol{\nabla}\cdot\rho\boldsymbol{v}\boldsymbol{v} = -\boldsymbol{\nabla}p \quad \text{(decoupled)}, & \text{(5a)} \\ \dfrac{\partial(\rho+\rho_{\rm c})\boldsymbol{v}}{\partial t} + \boldsymbol{\nabla}\cdot(\rho+\rho_{\rm c})\boldsymbol{v}\boldsymbol{v} = -\boldsymbol{\nabla}p \quad \text{(coupled)}, & \text{(5b)} \end{cases}$$

$$\frac{\partial e}{\partial t} + \boldsymbol{\nabla}\cdot e\boldsymbol{v} = -p\boldsymbol{\nabla}\cdot\boldsymbol{v} + c\rho\bar{\kappa}E - 4\rho\bar{\kappa}\sigma_{\rm sb}T^4 - Q_{\rm coll}, \tag{6}$$

$$\begin{cases} \rho_{\rm c}C_{\rm sil}\dfrac{\partial T_{\rm c}}{\partial t} = c\rho_{\rm c}\kappa_{\rm c}E - 4\rho_{\rm c}\kappa_{\rm c}\sigma_{\rm sb}T_{\rm c}^4 \\ \quad + Q_{\rm coll} \quad \text{(decoupled)}, & \text{(7a)} \\ \dfrac{\partial}{\partial t}(\rho_{\rm c}C_{\rm sil}T_{\rm c}) + \boldsymbol{\nabla}\cdot(\rho_{\rm c}C_{\rm sil}T_{\rm c})\boldsymbol{v} = c\rho_{\rm c}\kappa_{\rm c}E \\ \quad - 4\rho_{\rm c}\kappa_{\rm c}\sigma_{\rm sb}T_{\rm c}^4 + Q_{\rm coll} \quad \text{(coupled)}, & \text{(7b)} \end{cases}$$

$$\frac{\partial E}{\partial t} + \boldsymbol{\nabla}\cdot\boldsymbol{F} = 4\rho\bar{\kappa}\sigma_{\rm sb}T^4 + 4\rho_{\rm c}\kappa_{\rm c}\sigma_{\rm sb}T_{\rm c}^4 - c\rho\bar{\kappa}E - c\rho_{\rm c}\kappa_{\rm c}E, \tag{8}$$

where ρ, $\boldsymbol{v}$, e, p, and T are the (mass) density, velocity, internal energy density, pressure, and temperature, respectively. The subscript c indicates those parameters for chondrules (e.g., $\rho_{\rm c}$ and $T_{\rm c}$), and the subscript zero indicates the initial value. From Equations (3)–(8), gas (both nebula hydrogen molecules and silicate vapor) and small dust grains are combined into a single fluid under the assumption that they are dynamically and thermally well coupled to each other. Hereafter, we refer to this combined fluid as dusty gas, and the bar on the variables indicates the average of the gas and dust mixture in this paper. The right-hand sides of Equations (6) and (7) include the terms of the emission and absorption of the radiation. The speed of light is c, and the Stefan–Boltzmann constant is $\sigma_{\rm sb}$. The opacities $\bar{\kappa}$ and $\kappa_{\rm c}$ are those of dusty gas and chondrules, respectively. We also simultaneously solve the radiation energy density E and radiation energy flux $\boldsymbol{F}$ in Equation (8). The terms of the (hydrodynamic) advection of the radiation energy and the rate of the work done by the radiative pressure are omitted from Equation (8) because the typical velocity of the dynamics is orders of magnitude less than c/τ (τ is the optical depth), and the dynamical diffusion limit (Stone et al. 1992) never appears. The equations of state are formulated as follows:

$$p = p_{\mathrm{H_2}} + p_{\mathrm{sil}}, \tag{9}$$

$$e = (\rho_{\mathrm{H_2}} C_{\mathrm{H_2}} + \rho_{\mathrm{d}} C_{\mathrm{sil}})T = \rho \bar{C} T, \tag{10}$$

where $\rho_{\mathrm{H_2}}$ is the density of the hydrogen molecules; ρ_{d} is the density of the dust grains, including the vapor evaporated from them; and $p_{\mathrm{H_2}}$ and p_{sil} are the partial pressures of the hydrogen molecules and evaporated silicate vapor. We consider the evaporation of dust grains but ignore the evaporation of chondrules in this study. This is because we need to properly treat the mixing of the materials between dust grains and chondrules via recondensation, which is hard to numerically calculate as it is lacking in the model and data, for the consideration of the evaporation of both dust grains and chondrules. At the initial state, dust grains have a larger surface area per unit volume than chondrules; therefore, dust grains might preferentially evaporate. The heat capacity of hydrogen molecules $C_{\mathrm{H_2}}$ is calculated from the ideal gas law. We adopt the same values of the heat capacities for the solid silicate particles and the evaporated vapor as $C_{\mathrm{sil}} = 10^7$ erg g^{-1} K^{-1} for simplicity. We also ignore the latent heat of the phase transitions. In Equations (6) and (7), Q_{coll} denotes the energy transfer between dusty gas and chondrules due to the thermal collision.

The initial condition is described as follows:

$$\rho(r) = \rho_0, \tag{11}$$

$$\rho_{\mathrm{c}}(r) = \rho_{\mathrm{c},0}, \tag{12}$$

$$\boldsymbol{v}(r) = 0, \tag{13}$$

$$\begin{cases} T_{\mathrm{peak}} \quad (r < r_{\mathrm{dis}}), & \text{(14a)} \\ T_0 \quad (r > r_{\mathrm{dis}}), & \text{(14b)} \end{cases}$$

$$\begin{cases} \dfrac{4\sigma_{\mathrm{sb}} T_{\mathrm{peak}}^4}{c} \quad (r < r_{\mathrm{dis}}), & \text{(15a)} \\ \dfrac{4\sigma_{\mathrm{sb}} T_0^4}{c} \quad (r > r_{\mathrm{dis}}), & \text{(15b)} \end{cases}$$

where r is the distance from the central axis of the cylindrical column. The initial density fields are uniformly distributed. We assume $\rho_{\mathrm{c},0} = 10^{-4}$ g cm^{-3} as the fiducial chondrule density, which is the middle of the solid density expected by Alexander et al. (2008), and $\rho_{\mathrm{d},0} = 10^{-5}$ g cm^{-3} as the fiducial dust density, which is one-tenth of the fiducial chondrule density. We set the fiducial nebula gas density as $\rho_{\mathrm{H_2},0} = 10^{-10}$ g cm^{-3}, the typical value in the asteroid belt region in the minimum-mass solar nebula model (Hayashi 1981). The initial dusty gas density is $\rho_0 = \rho_{\mathrm{d},0} + \rho_{\mathrm{H_2},0}$. In this paper, the initial ambient nebula temperature T_0 is fixed at 200 K. The peak temperature in the hot channel T_{peak} is a free parameter, and its fiducial value is 2000 K.

Our calculations start from the condition that the channel reaches the peak temperature, and the discharge currents cease. We assume that the duration of the discharge is negligibly short and ignore the temporal energy release from the discharge currents. This may not necessarily be a realistic assumption, while there are many uncertainties in the discharge process in protoplanetary disks. Johansen & Okuzumi (2018) predicted a duration of ~100 s from the duration of the flashes in the terrestrial lightning following the Townsend law (e.g., Ebert et al. 2010).

If we ignore the dynamics of the discharge channel, the radiative diffusion timescales are

$$t_{\mathrm{rad}} \sim \frac{3\kappa_{\mathrm{d}}\rho_{\mathrm{d}}\rho_{\mathrm{c}} C_{\mathrm{sil}} r_{\mathrm{dis}}^2}{64\pi^2 \sigma_{\mathrm{SB}} T^3} \sim 1.4\ \mathrm{hr} \left(\frac{\rho_{\mathrm{d}}}{10^{-5}\ \mathrm{g\ cm^{-3}}}\right)^{-1} \left(\frac{\rho_{\mathrm{c}}}{10^{-4}\ \mathrm{g\ cm^{-3}}}\right)^{-1} \times \left(\frac{r_{\mathrm{dis}}}{1\ \mathrm{km}}\right)^{2} \left(\frac{T}{1600\ \mathrm{K}}\right)^{-3} \tag{16}$$

for our fiducial parameters (Desch & Connolly 2002), where κ_{d} is the dust opacity (see Equation (24) in Section 3.2). The corresponding cooling rates of chondrules residing in the channel are within the desired range of ~10–10^3 K hr^{-1}. However, the expansion of the channel might make their cooling faster than that of the static channel. Therefore, we reexamine the cooling rates of chondrules predicted by the lightning model considering the dynamics of the channel. It could benefit the future study of compound chondrule formation, chemical evolution, and so on accompanying chondrule-forming events because the dynamics takes key roles for these phenomena.

We also implicitly assume that there are chondrule-forming events of ordinary chondrites, which might have been formed inside the water snowline, and therefore do not consider the evaporation of the volatile species. The expected contributions of the volatile species and chondrule-forming events of carbonaceous chondrites are discussed in Section 5.5.

The next section explains the method to solve Equations (3)–(10). The key variables in this paper are summarized in Table 1. We show a schematic picture of our model in Figure 1. Our problem is on a 1D axisymmetric cylindrical coordinate system.

Table 1
List of Key Variables

Variable	Meaning
$\rho_{\mathrm{H_2}}$	Density of gas (hydrogen molecules)
ρ_{d}	Density of dust grains and silicate vapor
ρ	Density of dusty gas: $\rho_{\mathrm{H_2}} + \rho_{\mathrm{d}}$
ρ_{c}	Density of chondrules
r_{dis}	Radius of the discharge channel; also the initial radius of the hot column
T	Temperature of dusty gas
T_{c}	Temperature of chondrules
T_{peak}	Peak temperature of chondrules; also the initial temperature of the hot column
$p_{\mathrm{H_2}}$	Partial pressure of gas
p_{sil}	Partial pressure of silicate vapor
p	Total pressure: $p_{\mathrm{H_2}} + p_{\mathrm{sil}}$
a_{c}	Radius of chondrule fixed at 0.3 mm
a_{d}	Radius of dust grains 1 μm without the evaporation
v	Radial velocity of the dusty gas
t	Time

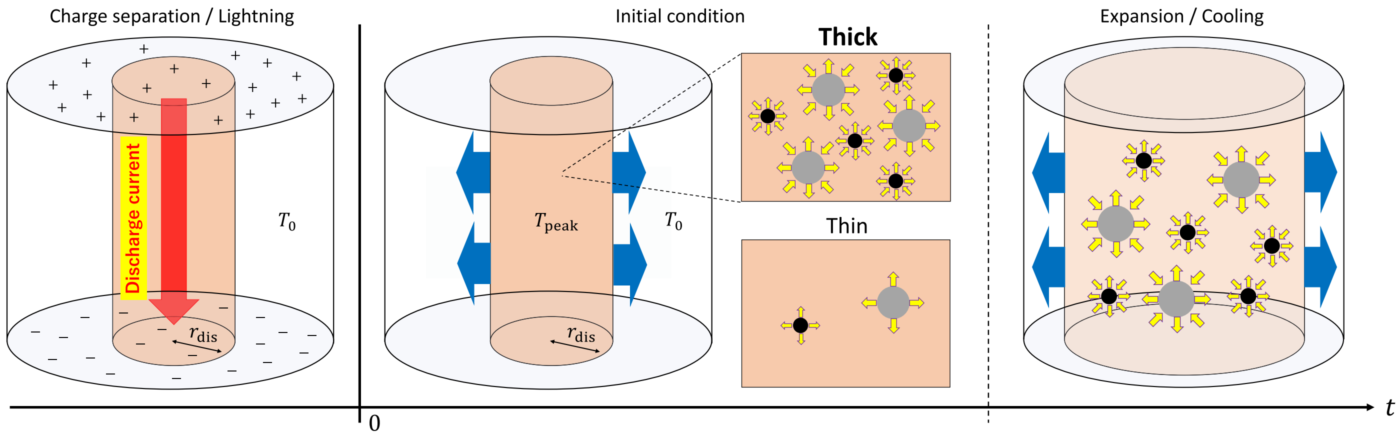

Figure 1. Schematic picture of our model. We do not treat the processes to separate the charges and generate the lightning in protoplanetary disks (left). We focus on the thermal histories of chondrules in the hot discharge channel (cylinder) after the release of the energy stored in the electric field via the lightning. At the initial state, the hot cylindrical channel filled with chondrules (gray larger circles) and dust grains (black smaller circles) at the peak temperature is assumed (center). We calculate the dynamical evolution of the channel and the thermal evolution of the chondrules inside it. The hot channel expands due to a higher pressure than that of the ambient nebula gas (blue arrows). Chondrules cool down by their thermal radiation (yellow arrows pointing outward). Under the optically thin condition, the cooling rates of the chondrules are too fast to reproduce the textures of the chondrules because the radiation freely escapes into space. However, under the optically thick condition, chondrules absorb the radiation emitted from the neighborhood chondrules and dust grains (yellow arrows pointing to chondrules), so the cooling rates of the chondrules can be slower than the optically thin condition and proper to reproduce the actual chondrules. The fainter color of the column (right) indicates the cooling of the chondrules and dust grains inside the channel.

3. Method

We solve Equations (3)–(10) using the finite-difference method. Our method is built on the algorithm of the Eulerian hydrodynamics code ZEUS (Stone & Norman 1992). Our calculation domain is divided into the static cells, and the variables that appear in Equations (3)–(10) are defined at either the cell center or cell interface. Equations (3)–(10) contain four parts: hydrodynamics, radiative transfer, thermal collision, and evaporation. We divide these four parts into five steps, described below (only the hydrodynamics part comprises the transport and source steps, and the other parts have the corresponding steps). We adopt the operator splitting method of the ZEUS code to integrate all of the steps. All but the radiative transfer step are solved explicitly. Figure 2 shows the flowchart of our calculation during one time step.

3.1. Hydrodynamics Transport and Source Step

The hydrodynamics part is performed using the original algorithm of the ZEUS code, which comprises the transport and source steps. The hydrodynamics part determines the time increment dt during each time step from the Courant–Friedrichs–Lewy condition.

3.2. Radiative Transfer Step

The radiative transfer step is performed implicitly because the timescale of the radiative transfer is much smaller than the hydrodynamics timescale. The following equations are solved during this step:

$$\rho\bar{C}\left(\frac{T^{l+1}-T^{l}}{dt}\right) = c\rho\bar{\kappa}E^{l+1} - 4\rho\bar{\kappa}\sigma_{\rm sb}(T^{l+1})^4, \tag{17}$$

$$\rho_{\rm c}C_{\rm sil}\left(\frac{T_{\rm c}^{l+1}-T_{\rm c}^{l}}{dt}\right) = c\rho_{\rm c}\kappa_{\rm c}E^{l+1} - 4\rho_{\rm c}\kappa_{\rm c}\sigma_{\rm sb}(T_{\rm c}^{l+1})^4, \tag{18}$$

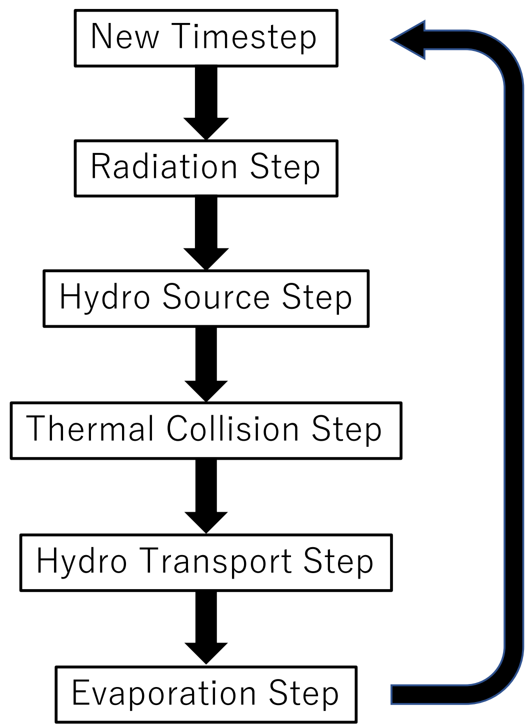

Figure 2. Flowchart of our simulation scheme: one cycle for each time step. We confirmed that the order of the steps does not affect the results.

$$\frac{E^{l+1}-E^{l}}{dt} + \nabla\cdot\boldsymbol{F}^{l+1} = 4\rho\bar{\kappa}\sigma_{\rm sb}(T^{l+1})^4 + 4\rho_{\rm c}\kappa_{\rm c}\sigma_{\rm sb}(T_{\rm c}^{l+1})^4 - c\rho\bar{\kappa}E^{l+1} - c\rho_{\rm c}\kappa_{\rm c}E^{l+1}. \tag{19}$$

In Equations (17)–(19), the superscripts l and $l+1$ on the variables indicate the time step; l means the present step, and $l+1$ means the next step. The terms with the fourth power of the temperature are approximately linearized as follows:

$$(T^{l+1})^4 = 4(T^l)^3T^{l+1} - 3(T^l)^4. \tag{20}$$

To ensure the validity of this approximation, the radiative transfer step is subdivided into 10^I substeps with a time increment of $dt/10^I$, where I is an integer large enough for the changes in the temperatures to be less than 1 % at all of the cells after the single substep. The number I is found for each time step. We confirm that $I \leqslant 1$ except only at the early time of the calculations affected by the artificial discontinuity at $r = r_{\rm dis}$, and we do not have to worry about this issue. The radiative energy flux $\boldsymbol{F}$ is evaluated by adopting the flux-limited diffusion (FLD) approximation,

$$\boldsymbol{F} = \frac{\lambda c}{\rho\bar{\kappa} + \rho_{\rm c}\kappa_{\rm c}}\boldsymbol{\nabla} E, \tag{21}$$

where the flux limiter λ is evaluated as follows:

$$\lambda = \frac{2 + R}{6 + 3R + R^2}, \tag{22}$$

$$R = \frac{|\boldsymbol{\nabla} E|}{(\rho\bar{\kappa} + \rho_{\rm c}\kappa_{\rm c})E}. \tag{23}$$

In this study, the geometric opacities of the solid dust grains $\kappa_{\rm d}$ and chondrules $\kappa_{\rm c}$ are calculated from their radius $a_{\rm d}$ and $a_{\rm c}$, respectively,

$$\kappa_{\rm d} = \frac{\pi a_{\rm d}^2}{4/3\pi a_{\rm d}^3\rho_{\rm mat}} = 2.5 \times 10^3 \text{ cm}^2 \text{ g}^{-1}\left(\frac{a_{\rm d}}{1\ \mu\text{m}}\right)^{-1}, \tag{24}$$

$$\kappa_{\rm c} = \frac{\pi a_{\rm c}^2}{4/3\pi a_{\rm c}^3\rho_{\rm mat}} = 8.3 \text{ cm}^2 \text{ g}^{-1}\left(\frac{a_{\rm c}}{0.3\text{ mm}}\right)^{-1}, \tag{25}$$

where $\rho_{\rm mat}$ is the material density of the silicate particles and set to be $3.0\,\text{g cm}^{-3}$ in this study. The average opacity of the dusty gas $\bar{\kappa}$ is calculated as follows:

$$\bar{\kappa} = \frac{(1 - f_{\rm evap})\rho_{\rm d}\kappa_{\rm d}}{\rho_{\rm d} + \rho_{\rm H_2}}, \tag{26}$$

where $f_{\rm evap}$ is the evaporated fraction of dust grains. While the peak wavelength of the blackbody radiation at the temperature range relevant to chondrule formation is close to the dust radius ($\approx$1 μm) and shorter than the chondrule radius ($\approx$0.3 mm), olivine and pyroxene, which are the main constituents of chondrules, actually have low absorption coefficients compared to the perfect blackbody (e.g., Eisenhour et al. 1994). However, opaque inclusions such as troilite, magnetite, and Fe–Ni metal grains also exist. So we consider only the geometric opacity for simplicity here. The cooling rates of chondrules are inversely proportional to the absorption coefficients; e.g., 10 times lower opacities result in 10 times higher cooling rates, which can be compensated for by a three times larger discharging radius or solid densities (see Subsection 5.2).

We set the negligibly small values for the opacities of the gas species, hydrogen molecules, and silicate vapor. We note that, in most cases, our calculation domain is optically thick, so the diffusion limit of the FLD approximation is applied.

3.3. Thermal Collision Step

The energy transfer due to the thermal collision, $Q_{\rm coll}$ in Equations (6) and (7), is described as follows (e.g., Iida et al. 2001):

$$\begin{aligned} Q_{\rm coll} &= 4\pi a_{\rm c}^2 n_{\rm c} q_{\rm a} \\ &= 4\pi a_{\rm c}^2 n_{\rm c}\sum_i \frac{1}{8\sqrt{\pi}}\rho_i(T - T_{\rm c})\frac{\gamma_i + 1}{\gamma_i - 1}\left(\frac{2k_{\rm B}}{m_i}\right)^{3/2}\sqrt{T}, \end{aligned} \tag{27}$$

where ρ_i, m_i, and γ_i are the density, molecular (or atomic) mass, and ratio of the specific heats for the species i, which includes hydrogen molecules and the evaporated species from the silicate particles, Mg, SiO, and O_2 (see also evaporation step). The Boltzmann constant is $k_{\rm B}$. The number density of chondrules is $n_{\rm c}$, and the heat transfer rate per unit chondrule surface area is $q_{\rm a}$. We ignore the drag heating. The thermal collision step is performed at each cell of the domain by solving the closed system equations below and assuming constant density during this step:

$$\rho\bar{C}\frac{dT}{dt} = -Q_{\rm coll}, \tag{28}$$

$$\rho_{\rm c} C_{\rm sil}\frac{dT_{\rm c}}{dt} = Q_{\rm coll}. \tag{29}$$

From Equation (27) and the preservation of the total energy of the system, we have the analytical solution to the thermal collision step:

$$\sqrt{T^{l+1}/T_\infty} = \frac{-1 + \left(\frac{1 + \sqrt{T^l/T_\infty}}{1 - \sqrt{T^l/T_\infty}}\right)\exp[Adt]}{1 + \left(\frac{1 + \sqrt{T^l/T_\infty}}{1 - \sqrt{T^l/T_\infty}}\right)\exp[Adt]}, \tag{30}$$

where

$$T_\infty = \frac{e_{\rm sum}}{\rho\bar{C} + \rho_{\rm c} C_{\rm sil}}, \tag{31}$$

and

$$\begin{aligned} A = &\frac{e_{\rm sum}}{\rho\bar{C}\cdot\rho_{\rm c} C_{\rm sil}\sqrt{T_\infty}} \\ &\times 4\pi a_{\rm c}^2 n_{\rm c}\sum_i \frac{1}{8\sqrt{\pi}}\rho_i\frac{\gamma_i + 1}{\gamma_i - 1}\left(\frac{2k_{\rm B}}{m_i}\right)^{3/2}, \end{aligned} \tag{32}$$

in which $e_{\rm sum}$ is the sum of the energy of dusty gas and chondrules,

$$e_{\rm sum} = \rho\bar{C}T^l + \rho_{\rm c} C_{\rm sil} T_{\rm c}^l = \rho\bar{C}T^{l+1} + \rho_{\rm c} C_{\rm sil} T_{\rm c}^{l+1}. \tag{33}$$

3.4. Evaporation Step

For simplicity, we do not solve the evaporation and condensation rate equations. Instead, we assume that either an equilibrium state or complete evaporation is achieved. Then, the silicate vapor pressure $p_{\rm sil}$ is formulated as follows:

$$p_{\rm sil} = \min\left[p_{\rm sil}^{\rm eq}, \rho_{\rm d}\left(\frac{k_{\rm B}T}{\bar{m}_{\rm Fo}}\right)\right], \tag{34}$$

where $p_{\rm sil}^{\rm eq}$ is the equilibrium pressure of silicate vapor, and $\bar{m}_{\rm Fo}$ is the average molecular mass of the evaporated species. Assuming the following chemical reaction and the congruent

Table 2
List of Run Names

Name	r_{dis} (km)	$\rho_{c,0}$ (g cm^{-3})	$\rho_{g,0}$ (g cm^{-3})	$\rho_{d,0}/\rho_{c,0}$	T_{peak} (K)	Evaporation of Dust Yes or No
Decoupled						
d1	1	10^{-5}	10^{-10}	0.1	2000	Yes
d2 (fiducial)	1	10^{-4}	10^{-10}	0.1	2000	Yes
d02	1	10^{-4}	10^{-10}	0.1	2000	No
d3	10	10^{-5}	10^{-10}	0.1	2000	Yes
d4	1	10^{-4}	10^{-11}	0.1	2000	Yes
d5	1	10^{-4}	10^{-10}	0.5	2000	Yes
d6	1	10^{-4}	10^{-10}	0.1	2200	Yes
Coupled						
c1	1	10^{-5}	10^{-10}	0.1	2000	Yes
c2 (fiducial)	1	10^{-4}	10^{-10}	0.1	2000	Yes
c02	1	10^{-4}	10^{-10}	0.1	2000	No
c3	10	10^{-5}	10^{-10}	0.1	2000	Yes

evaporation of forsterite,

$$\mathrm{Mg_2SiO_4} \rightleftharpoons 2\,\mathrm{Mg} + \mathrm{SiO} + \frac{3}{2}\mathrm{O_2}, \tag{35}$$

Miura et al. (2002) obtained

$$p_{\mathrm{sil}}^{\mathrm{eq}}(T) = 3.24 \times 10^8 \exp\left[-\frac{61{,}800\ \mathrm{K}}{T}\right]\ \mathrm{atm}. \tag{36}$$

The actual equilibrium pressure of silicate vapor must differ from and be more complicated than Equation (36). It depends on the composition of chondrule precursors and chondrule-forming environments. The equilibrium pressure of forsterite itself depends on the pressure of hydrogen molecules (e.g., Tsuchiyama et al. 1999). Although Equation (36) is without hydrogen molecules and unrealistic for chondrule-forming environments, the usages of Equation (36) capture the fundamental importance of the vapor pressure of silicate on the dynamics of dusty gas and the thermal histories of chondrules. The size of the dust grains is updated after the evaporation step, assuming no production and loss in the number density of the grains. From Equation (34), we have the evaporated fraction f_{evap} from the original dust grains. Then, the volume of the condensed dust grains is $1 - f_{\mathrm{evap}}$ times that of the original ones. The size of the dust grains is calculated accordingly. Without the evaporation, the original dust grains have $a_{\mathrm{d}} = 1\ \mu$m. We fix the size of the chondrules at $a_{\mathrm{c}} = 0.3$ mm.

3.5. Domain Size, Grid Number, Boundary Condition, and Simulation Time

Our calculation domain has a range of $0 \leqslant r \leqslant 100\, r_{\mathrm{dis}}$. We divide the inner domain ($0 \leqslant r \leqslant 10 r_{\mathrm{dis}}$) into equally spaced 10,000 ($= N_{\mathrm{in}}$) cells and the outer domain ($10\, r_{\mathrm{dis}} \leqslant r \leqslant 100\, r_{\mathrm{dis}}$) into logarithmically spaced 2500 ($= N_{\mathrm{out}}$) cells. We confirm that the results obtained with these numbers of cells do not deviate from the results with both double (N_{in}, N_{out}) = (20,000, 5000) and half (N_{in}, N_{out}) = (5000, 1250) the number of cells. We set a zero flux (or reflecting) inner boundary condition and constant outer boundary condition. The values at the outer boundary are those of the ambient dusty gas, for example, $T = T_0$ and $\rho = \rho_0$ at the outer boundary. We confirm that the calculation domain is large enough for the outer boundary condition not to affect the results. We conduct the calculations until the temperature of the innermost chondrules drops below the solidus temperature T_{solid}. In this study, $T_{\mathrm{solid}} = 1400$ K is assumed.

4. Results

Table 2 shows the names of the runs and the corresponding parameter sets. We set runs d2 and c2 as the fiducial runs for the decoupled (Section 4.1) and coupled (Section 4.2) cases, respectively.

4.1. Decoupled Case

Figures 3–5 show the time evolution of our fiducial run d2, which demonstrates the three typical phases of the evolution: expansion (Figure 3), return (Figure 4), and pressure balance (Figure 5). The top panels show the dusty gas density ρ (blue solid line) and total pressure p (red dashed line), the middle panels show the radial velocity v (magenta solid lines for positive and violet dashed lines for negative), and the bottom panels show the temperatures of dusty gas T (brown dashed line) and chondrules T_{c} (black solid line). The dusty gas density includes nebula hydrogen molecules, silicate vapor, and solid small dust grains. The total pressure includes nebula hydrogen molecules and silicate vapor.

As shown in the top and middle panels of Figure 3, the information on the initial discontinuity at $r = r_{\mathrm{dis}} = 1$ km propagates outward and inward during the expansion phase. It reaches the column's central axis at around $t \simeq 100$ s, and after that, the density of dusty gas in the inner region significantly decreases. Despite the decrease in the density, the total pressure in the hot region within $r \lesssim r_{\mathrm{dis}}$ stays almost constant until $t \simeq 250$ s because the silicate vapor keeps the equilibrium pressure (Equation (36)) at an almost constant temperature (see the bottom panel of Figure 3) and dominates the total pressure. After $t \simeq 250$ s, the dust grains completely evaporate in the hot region, and the silicate vapor cannot keep equilibrium. Therefore, the total pressure decreases as the density does. The middle panel of Figure 3 shows that the velocity is positive during the expansion phase, and the dusty gas expands outward until $t \simeq 250$–300 s, when it begins to

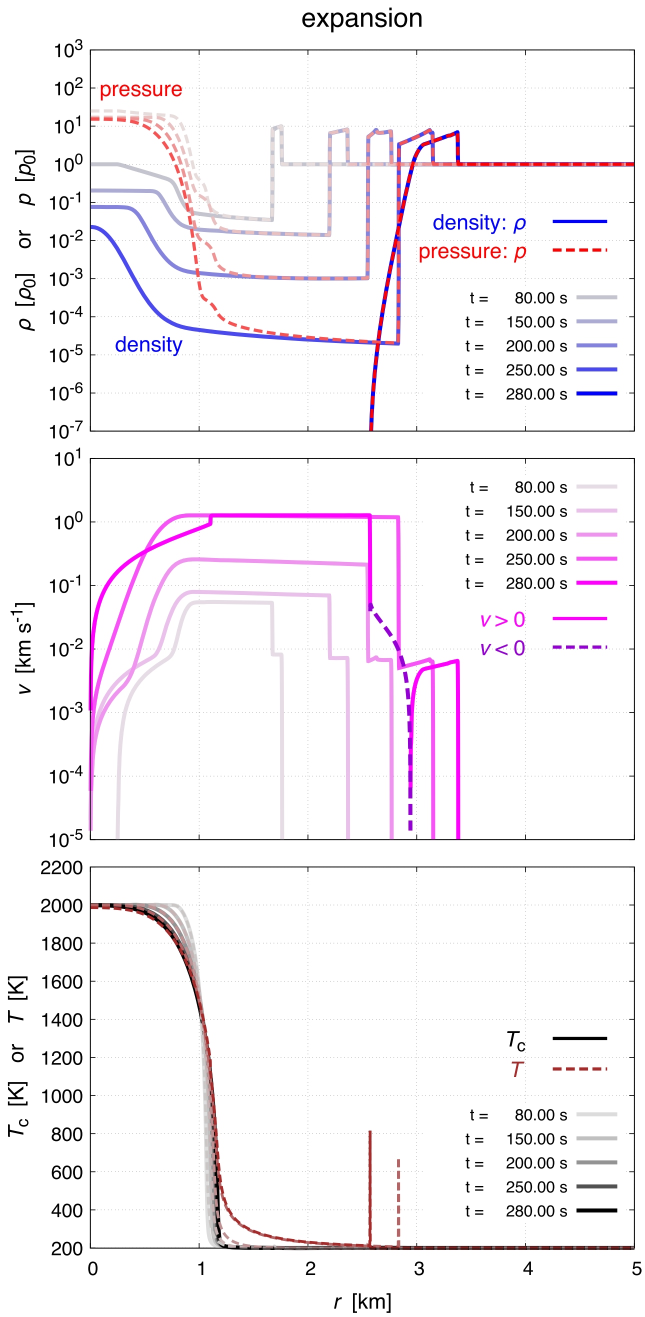

Figure 3. Time evolution of run d2 during the expansion phase. The top panel shows the evolution of the dusty gas density ρ (blue solid line) normalized by the ambient density ρ_0 and the total pressure p (red dashed line) normalized by the ambient pressure p_0. The middle panel shows the radial velocity of dusty gas v (the magenta solid line indicates $v > 0$, and the violet dashed line indicates $v < 0$). The bottom panel shows the dusty gas temperature T (brown dashed line) and chondrule temperature T_c (black solid line). The time proceeds from lighter- to darker-colored lines in each panel.

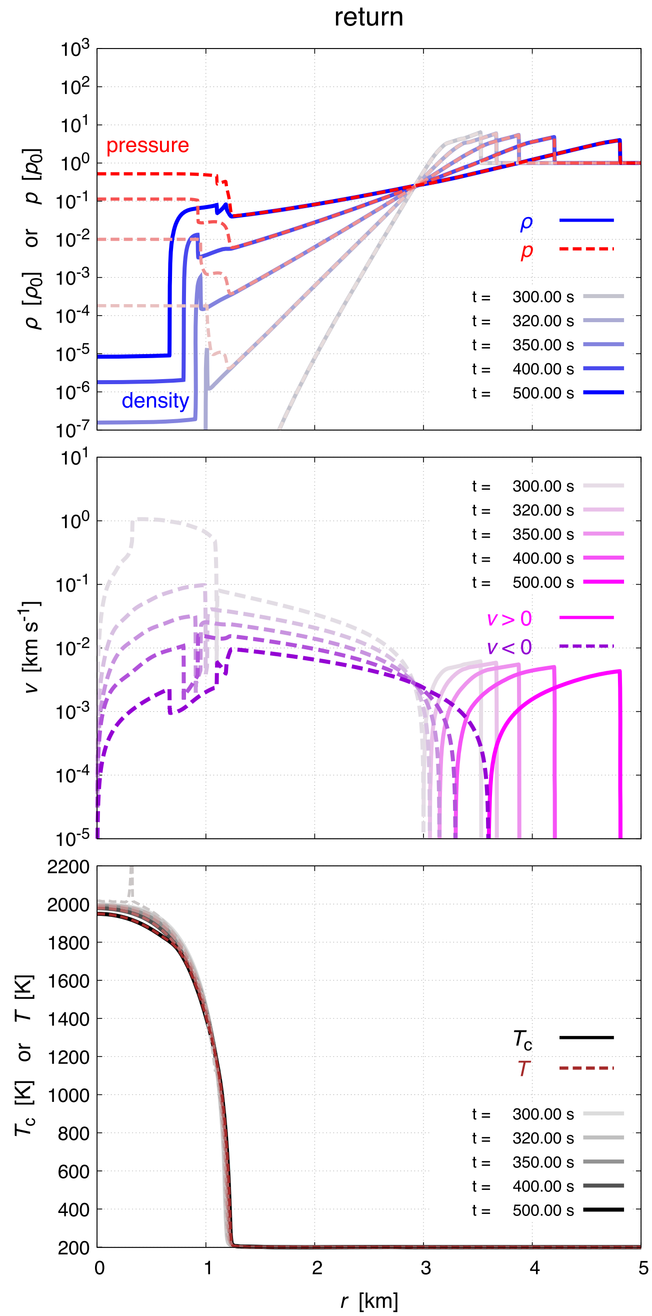

Figure 4. Time evolution of run d2 during the return phase. The meanings of the lines are similar to Figure 3.

return to the inner region. The temperature of the dusty gas T is almost equal to the temperature of the chondrules T_c throughout the entire evolution (bottom panels of Figures 3–5) due to the efficient energy exchange by the emission and absorption of the radiation or the thermal collision. Hot dusty gas expanding to outside the hot region is quenched by these processes buffered by the (not heated) chondrule precursors with a low temperature of T_0 because chondrules have a higher mass density and thus a higher energy density than dusty gas. We note that the work done by the hydrodynamics expansion and compression is negligible compared to the radiative transfer for the dusty gas because $e \gg p$. The needle-like structures appear at $t = 250$ and 280 s, locate at the interface between the positive and negative velocities, and propagate inward. This structure - vanishes soon after it reaches the central axis.

Figure 4 shows the return phase. The middle panel of Figure 4 shows that the velocity in the inner region is negative, and dusty gas returns to the hot region while the shock wave keeps spreading outward with positive velocity. As shown in the top panel of Figure 4, the density around the hot region recovers. However, the density within $r \lesssim r_{\rm dis}$ is still many orders of magnitude lower than the initial density because the

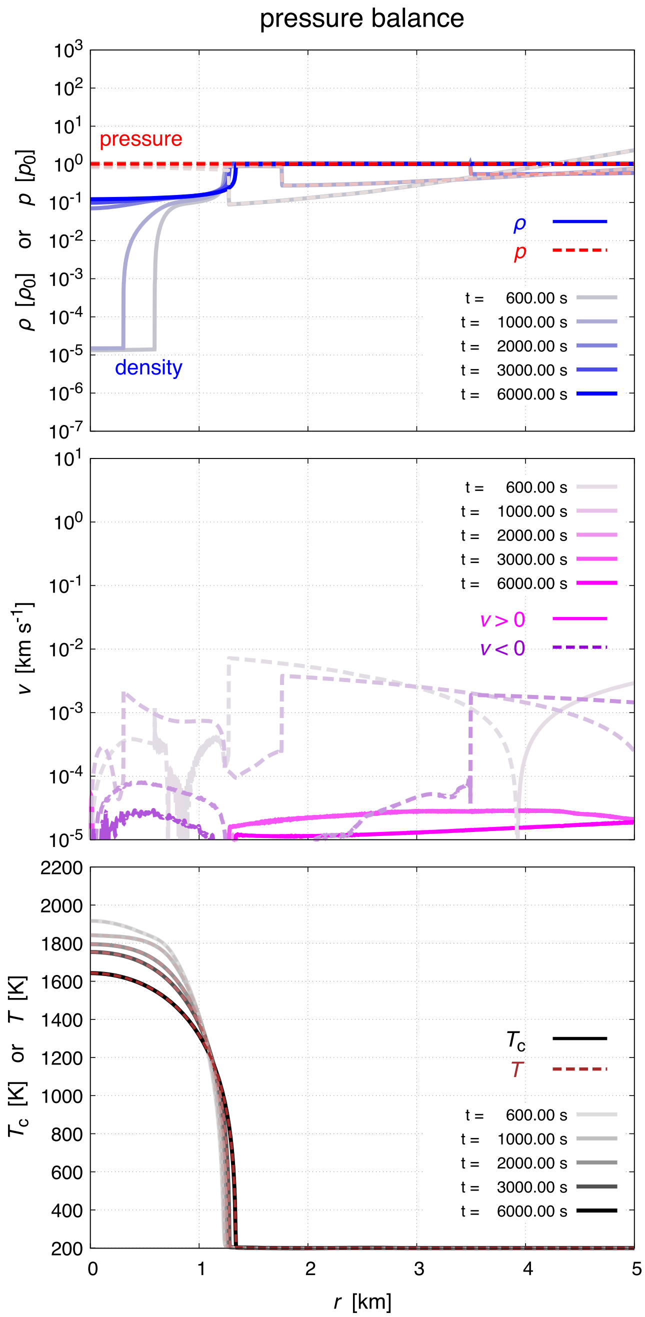

Figure 5. Time evolution of run d2 during the pressure balance phase. The meanings of the lines are similar to Figure 3.

vapor pressure of silicate prevents the materials from returning to this region.

After the return phase, the pressure balance is achieved, as shown in the top panel of Figure 5. However, until the temperature of the dusty gas drops so that the vapor pressure of the evaporated silicate grains is negligible compared to the pressure of hydrogen molecules, $p_{\rm sil}^{\rm eq} < p_{\rm H_2}$, the density in the heated region does not recover. The transition from $p_{\rm sil}^{\rm eq} > p_{\rm H_2}$ to $p_{\rm sil}^{\rm eq} < p_{\rm H_2}$ occurs between $t \simeq 1000$ and 2000 s and around $T \simeq 1800$ K.

To elucidate the effects of the evaporation of silicate dust on the dynamics, we compare the results above to those from a run without the evaporation. Figure 6 shows the time evolution of run d02 with the same parameter set as run d2 except for the evaporation of silicate dust (see Table 2). While the evolution sequence from the expansion phase to the pressure balance phase is a common feature of both runs, the significant decrease in the density of dusty gas does not occur in run d02. Moreover, the total pressure decreases with the density during the expansion phase because the vapor pressure of silicate is not taken into account. Therefore, the vapor pressure of silicate affects the density distribution and the transport of the materials in the hot region.

The cooling rates of chondrules expected from the models are key to judging whether the models can be reliable candidates for the chondrule-forming events. Now, we look at the cooling rates in the decoupled case.

The left panels of Figure 7 show the cooling rates of chondrules for runs d1, d2, and d3 (top to bottom). In the left panel of Figure 7(b) for our fiducial run d2, the cooling rates of chondrules suddenly drop from $\sim 10^3$ to $\sim 10^2$ K s^{-1}. This transition happens when the dusty gas returns to the hot region. The triangle ($t = 400$ s) and square ($t = 1500$ s) in Figure 7(b) represent the moments before and after the transition. The right panel of Figure 7(b) shows the corresponding density and temperature distributions at each moment. At $t = 400$ s, the chondrules determine the optical depth of the heated region because $\rho_c \gg \rho$ (hereafter the chondrule-dominated optical depth regime), while at $t = 1500$ s, the small dust grains with a larger opacity than the chondrules in the returning dusty gas determine the depth (hereafter the dust-dominated optical depth regime). As a result, the cooling rates at $t = 1500$ s are slower than at $t = 400$ s. The drop in the cooling rates coincides with the completion of the return phase. The cooling rates of chondrules after the transition to the dust-dominated optical depth regime are within the value of 10^1–10^3 K s^{-1}, which was expected from the laboratory experiments.

The left panel of Figure 7(a) shows the cooling rates of chondrules for run d1 with one-tenth the chondrule density $\rho_{\rm c,0}$ as run d2 (note the same $\rho_{\rm d,0}/\rho_{\rm c,0}$), and there is no drop in the cooling rates because the return phase does not complete before the chondrules solidify from melts at $t \simeq 60$ s, as indicated in the right panel of Figure 7(a). Overall, the cooling rates of 10^4–10^5 K s^{-1} are 10–100 times faster than run d2 because the lower density results in a lower optical depth; therefore, the radiation escapes more easily.

The same cooling rates as those from run d2 can be expected from the different sets of parameters. One of the examples is run d3, which is shown in Figure 7(c). We can observe a similar drop in the cooling rates as in run d2 from the left panel of Figure 7(c), and it coincides with the transition from the chondrule-dominated optical depth regime to the dust-dominated optical depth regime, as shown in the right panel of Figure 7(c). We discuss the analytically expected cooling rates of chondrules in Section 5.

Figure 8 exhibits the dependence of the cooling rates on parameters other than $\rho_{\rm c,0}$ and $r_{\rm dis}$. Figure 8(a) shows the result from run d4 with one-tenth the ambient gas density $\rho_{\rm g,0}$ as run d2, Figure 8(b) shows the result from run d5 with a larger dust-to-chondrule density ratio $\rho_{\rm d,0}/\rho_{\rm c,0}$ than run d2, and Figure 8(c) shows the result from run d6 with a larger initial temperature $T_{\rm peak}$ than run d2. In runs d4 and d6, the drop of the cooling rate is delayed compared to run d2 because the initial expansion is stronger than that of run d2. This is due to the lower ambient gas pressure for run d4 and the larger vapor pressure of silicate for run d6, which result in the stronger

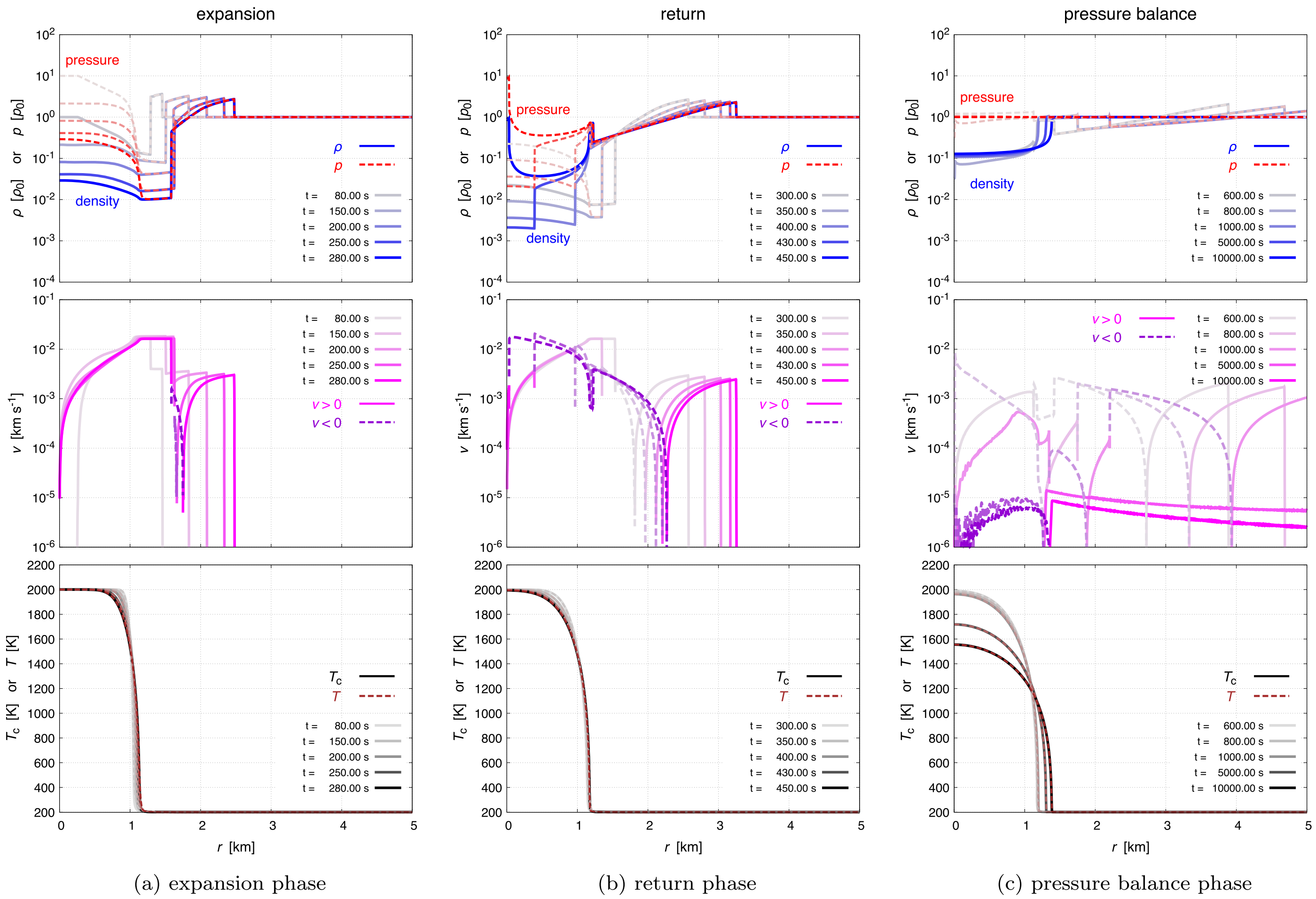

Figure 6. Time evolution of run d02. The left, middle, and right figures show the expansion, return, and pressure balance phases, respectively, and are arranged along the proceeding time. The meanings of the lines are similar to Figure 3.

expansion of the column and the delay in the completion of the return phase. In run d5, while before the drop of the cooling rates, this run expects the same cooling rates of 10^3–10^4 K s^{-1} as run d2, after the drop, the cooling rates of $\simeq 10^1$ K s^{-1} are almost 10 times slower than those of run d2. This is the consequence of the larger $\rho_{\rm d,0}/\rho_{\rm c,0}$ ratio, which only affects the dust-dominated optical depth regime.

4.2. Coupled Case

In this subsection, we present the results from the runs in the coupled case. The difference from the decoupled case is that the chondrules move with the surrounding dusty gas. Before proceeding, we need to explain how to track the trajectories and thermal histories of individual chondrules moving with dusty gas because our calculation code is Eulerian, and the variables are just defined at the static cell centers or interfaces. At first, we determine the positions of chondrules from the following mass conservation equation:

$$\int_0^{r[k](t)} 2\pi r \rho_{\rm c}(r) dr = \int_0^{r_0[k]} 2\pi r \rho_{\rm c,0} dr, \tag{37}$$

where $r[k](t)$ and $r_0[k]$ are the positions of the kth chondrules at t and the initial state, respectively. To the positions of $r[k](t)$, the variables, including the temperature, are linearly interpolated from the values at the neighborhood cells. An implicit assumption behind Equation (37) is that chondrules do not pass other chondrules.

Figure 9 shows the time evolution of our fiducial run c2, which demonstrates the same three typical phases as run d2: expansion, return, and pressure balance. In the top panels of Figure 9, the circles indicate the positions of chondrules that initially locate at $r_0 = 0.1 r_{\rm dis}$, $0.3 r_{\rm dis}$, $0.5 r_{\rm dis}$, $0.7 r_{\rm dis}$, and $0.9 r_{\rm dis}$ from left to right. During the expansion phase in Figure 9(a), the decrease in the density of dusty gas is very moderate compared to the decoupled case (Figure 3). The decrease in the total pressure is smaller than that in the density for the same reason as shown in the expansion phase of the decoupled case: the vapor pressure of silicate keeps the equilibrium pressure at an almost constant temperature and dominates the total pressure. Chondrules expanding outward are concentrated in the inner edge of the wall-like structure in the density distribution in the top panel of Figure 9(a). In the bottom panel of Figure 9(a), the hot region expands outward with hot chondrules, but we note that the total mass of chondrules in the hot region does not change. After the expansion phase, the chondrules concentrated in the wall-like structure return to the inner region (Figure 9(b)), and eventually, the pressure balance is achieved (Figure 9(c)).

To elucidate the effects of the evaporation of silicate dust, we compare the results of run c2 with those of a run without the evaporation. Figure 10 shows the time evolution of run c02

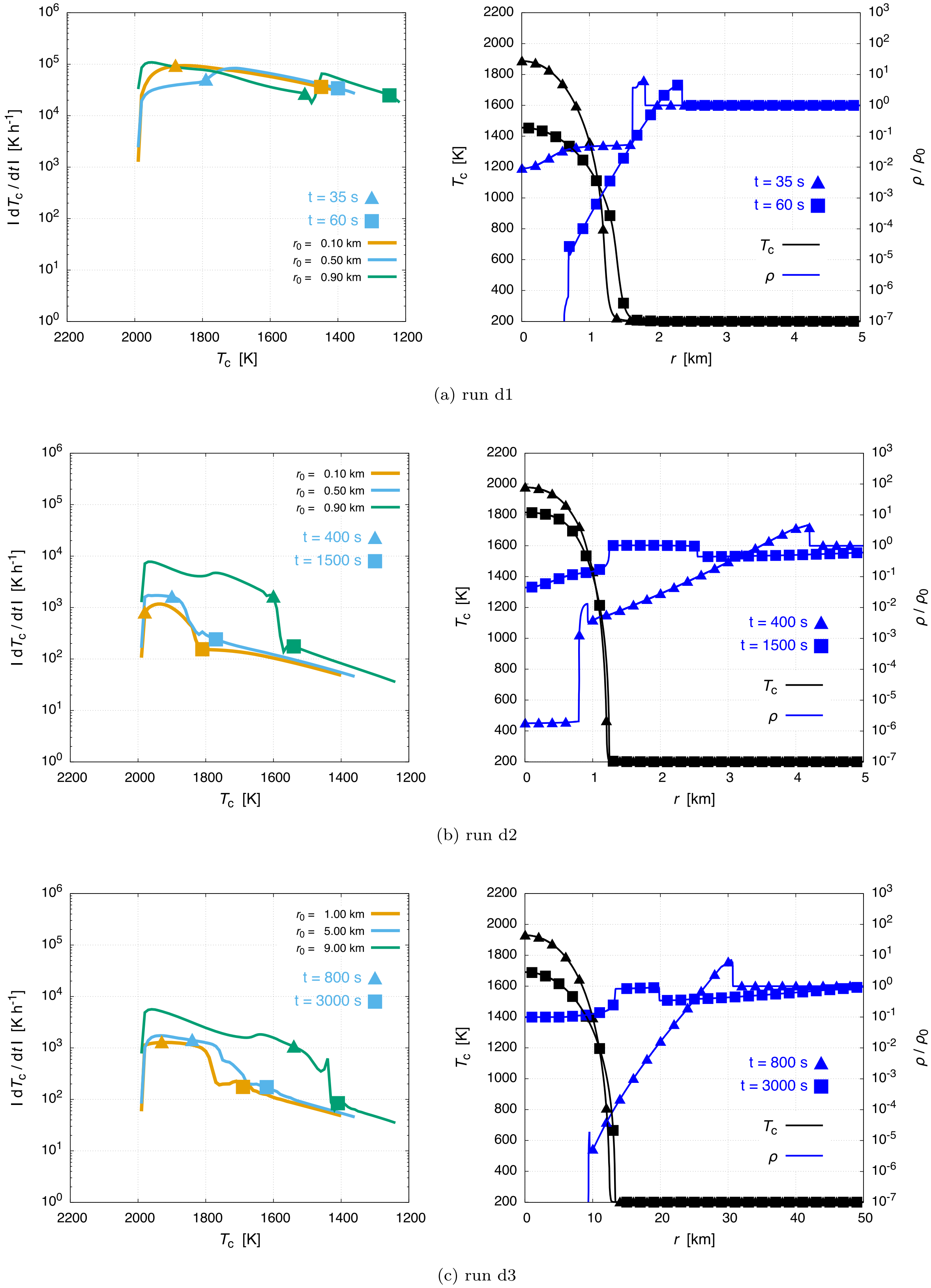

Figure 7. Left: cooling rates of chondrules for runs d1 (a), d2 (b), and d3 (c). The different colors of the lines indicate the different initial positions of the chondrules: $r_0 = 0.1r_{\rm dis}$ (orange), $0.5r_{\rm dis}$ (light blue), and $0.9r_{\rm dis}$ (green). The triangles and squares are plotted on the lines at two different moments shown in the figures. Right: snapshots of the density and temperature distributions. The blue and black solid lines indicate the distributions of the dusty gas density ρ and chondrule temperature T_c, respectively. The triangles and squares correspond to the same moments as shown in the left figures.

with the same parameter set as run c2 except for the evaporation. The appearance of the three phases is the ubiquitous outcome if the expanding materials can completely return to the inner region and the pressure balance can be achieved before the solidification of the chondrules. The most significant difference between runs c02 and c2 is that the

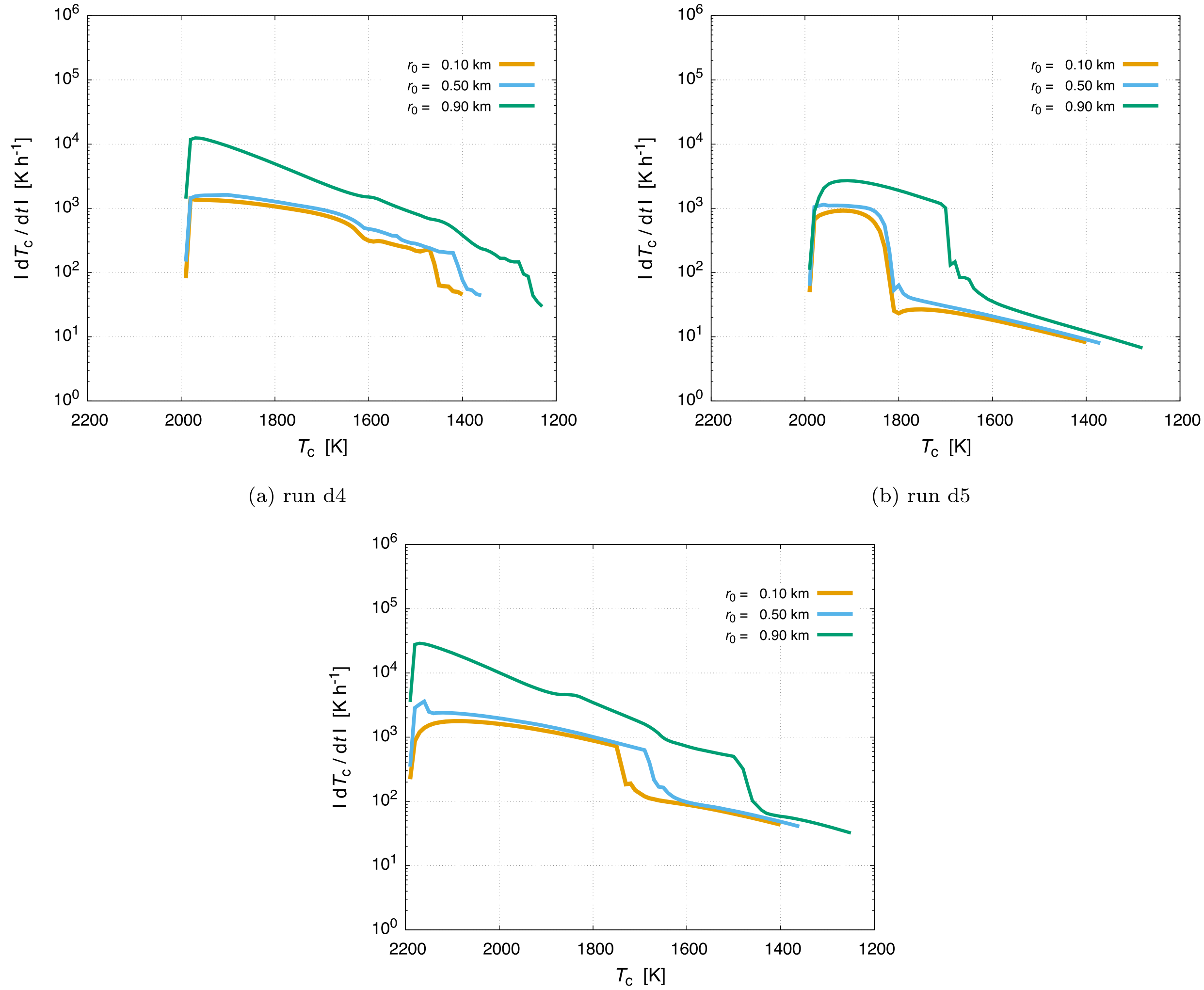

(a) run d4

(b) run d5

(c) run d6

Figure 8. Cooling rates of chondrules. Similar to the left panels of Figure 7.

chondrules are not concentrated in the wall-like structure and are equally spaced during the expansion phase in run c02.

We look at the cooling rates expected from the coupled case. The left panels of Figure 11 show the cooling rates of chondrules for runs c1, c2, and c3 (top, middle, and bottom, respectively). In the left panel of Figure 11(b) for run c2, the cooling rates of chondrules are within $\sim 10^2$–10^3 K s^{-1}, and run c2 predicts the proper cooling rates of chondrules. There is no sudden drop in the cooling rates seen in Figure 7, but the oscillation appears. In the coupled case, dust grains always dominate the optical depth unless they completely evaporate, so the transition from the chondrule-dominated regime to the dust-dominated regime never occurs. The right panels of Figure 11 show the migration of the chondrules, which exhibits the oscillation. This is the cause of the oscillation in the cooling rates. In Figure 11(b), at $t \simeq 1200$ s, the chondrules spread out to the local maxima, while at $t \simeq 3000$ s, they return to the local minima. During $1200\,\mathrm{s} \lesssim t \lesssim 3000$ s, the cooling rates drop and rise again (the lag is seen for $r_0 = 0.90$ km). As time proceeds, this oscillation is dampened, and finally, the pressure balance is achieved (see Figure 9(c)).

Figure 11(a) shows the results of run c1 with one-tenth the chondrule density of run c2. In the left panel of Figure 11(a), the cooling rates of chondrules are $\sim 10^4$ K s^{-1} and a little bit faster than the value expected from the experiments. The runs with the different parameter set from run c2 can also predict the desired cooling rates. Run c3 shown in Figure 11(c) is an example. We will discuss the analytical estimates of the cooling rates in Section 5 for both decoupled and coupled cases. We do not show the results of the additional runs to present the dependence on parameters other than $\rho_{c,0}$ and r_{dis}, such as ρ_{H_2}, $\rho_{d,0}/\rho_{c,0}$, and T_{peak}. They exhibit a similar evolution of the cooling rates as runs c1, c2, and c3. The impacts of these parameters are discussed in Section 5.

5. Discussion

5.1. Coupling of Chondrules

In this study, we consider two limiting cases for the dynamics of chondrules, the decoupled and coupled cases. This subsection evaluates how close to these extreme ones the lightning model's conditions are. We compare the typical timescale of the dynamics of the hot column and the stopping time of chondrules due to both gas and dust drag. We ignore the partial pressure of silicate vapor for simplicity. The typical

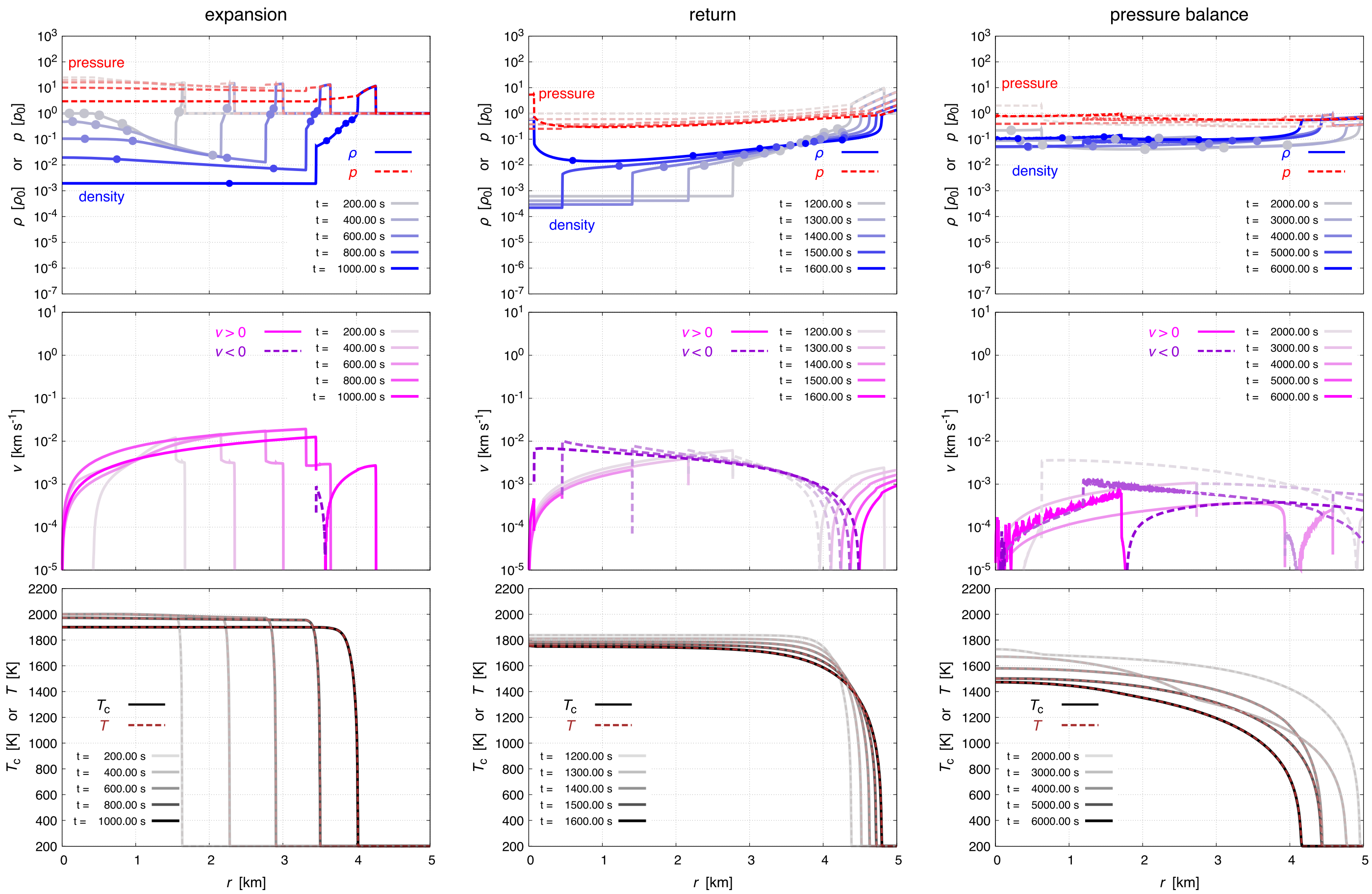

(a) expansion phase (b) return phase (c) pressure balance phase

Figure 9. Time evolution of run c2. Similar to Figure 6 but for run c2. In the top panels, the circles indicate the positions of chondrules that initially locate at $r_0 = 0.1r_{\rm dis}$, $0.3r_{\rm dis}$, $0.5r_{\rm dis}$, $0.7r_{\rm dis}$, and $0.9r_{\rm dis}$ from left to right.

velocity of the expansion of dusty gas is

$$v_{\rm typical} = c_{\rm s}\sqrt{\frac{\rho_{\rm H_2}}{\rho_{\rm H_2}+\rho_{\rm d}}}, \tag{38}$$

where $c_{\rm s}$ is the sound speed of pure hydrogen molecules. Then, the typical timescale of the dynamics is

$$t_{\rm typical} = \frac{r_{\rm dis}}{v_{\rm typical}} = \frac{r_{\rm dis}}{c_{\rm s}}\sqrt{\frac{\rho_{\rm H_2}+\rho_{\rm d}}{\rho_{\rm H_2}}}. \tag{39}$$

The stopping time of chondrules can be described as

$$t_{\rm stop} = \frac{m_{\rm c}v_{\rm typical}}{f_{\rm drag}}, \tag{40}$$

where $f_{\rm drag}$ is the total drag force, which is the summation of the contributions from hydrogen molecules,

$$f_{\rm drag,H_2} \sim \pi a_{\rm c}^2\rho_{\rm H_2}c_{\rm s}v_{\rm typical}, \tag{41}$$

and dust grains,

$$f_{\rm drag,d} \sim \pi a_{\rm c}^2\rho_{\rm d}v_{\rm typical}^2. \tag{42}$$

When $t_{\rm stop} \ll t_{\rm typical}$, chondrules must be well coupled to their surrounding dusty gas. Assuming $\rho_{\rm H_2} \ll \rho_{\rm d}$, this condition can be transformed into

$$\frac{t_{\rm stop}}{t_{\rm typical}} \sim \frac{m_{\rm c}}{\pi a_{\rm c}^2\rho_{\rm d}r_{\rm dis}} \sim 0.12\left(\frac{\rho_{\rm d}}{10^{-5}\ {\rm g\ cm^{-3}}}\right)^{-1}\left(\frac{r_{\rm dis}}{1\ {\rm km}}\right)^{-1}\left(\frac{a_{\rm c}}{0.3\ {\rm mm}}\right) \ll 1. \tag{43}$$

The dust drag $f_{\rm drag,d}$ is larger than the gas drag $f_{\rm drag,H_2}$ in Equation (43). As shown in the next subsection, the coupling of chondrules correlates with their cooling rates via a similar dependence on $\rho_{\rm d}$ and $r_{\rm dis}$. Equation (43) indicates that when the lightning model reproduces the proper cooling rates of chondrules, they are dragged by dusty gas, while the degree of the coupling might be at the transition between the two limiting cases. However, we note that we ignore the merger of small dust grains into chondrules. Chondrules must be hit by approximately the same mass of dust grains as their own before they stop against dusty gas. If small dust grains always

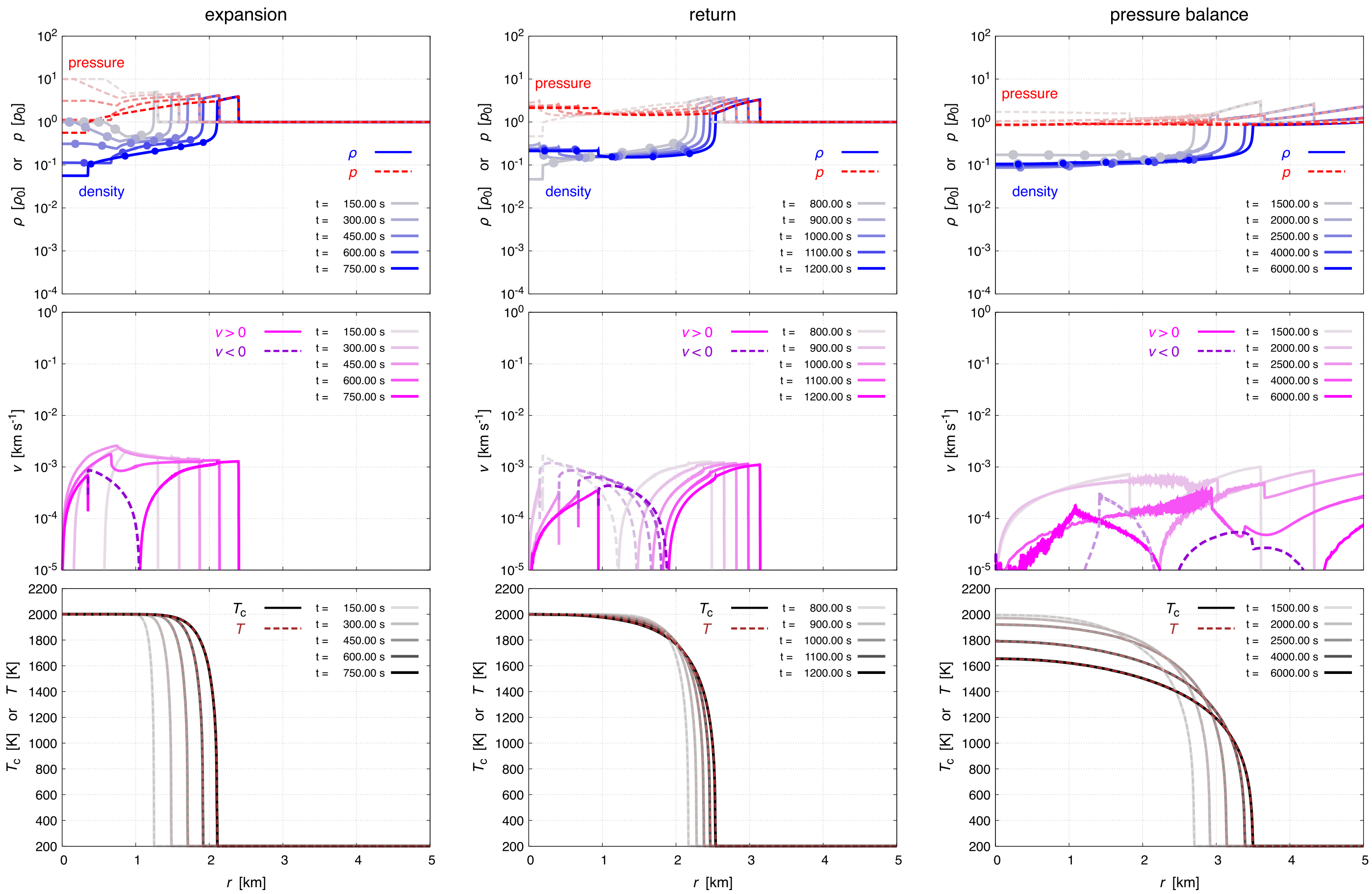

(a) expansion phase (b) return phase (c) pressure balance phase

Figure 10. Time evolution of run c02. Similar to Figure 9 but for run c02.

merge into chondrules, they might vanish before the chondrules are coupled to dusty gas.

5.2. Estimates of Cooling Rates

Chondrules lose their internal energy by thermal radiation but absorb the radiation energy emitted from the other chondrules. The cooling rates of chondrules are limited by the diffusion rates of the radiative energy at the interface between the hot inner region and the cold outer region. While chondrules also lose their energy by heat exchange with dusty gas via thermal collision, and dusty gas cools down by hydrodynamic expansion, cooling by these processes is negligible because $e \gg p$. We now analytically estimate the cooling rates of chondrules by radiative transfer.

We consider that chondrules that were initially located at the outer edge of the heated region $r = r_{\rm dis}$ expand to $r = r'$ at time t, where r' is the characteristic radius of the expanding hot column. In the decoupled case, $r' = r_{\rm dis}$ because the heated chondrules do not move. On the other hand, in the coupled cases, $r' \neq r_{\rm dis}$. The total mass of chondrules within $r \leqslant r'$ is constant,

$$M_{\rm c} = \int_0^{r'} 2\pi\rho_{\rm c} r h dr = \pi\rho_{\rm c,0} r_{\rm dis}^2 h, \tag{44}$$

where h is the length of the discharge channel or, in other words, the height of the cylindrical column. The radiative energy flux per unit area at $r = r'$ is

$$F' \sim \frac{\sigma_{\rm sb} T_c'^4}{\tau'}, \tag{45}$$

where T_c' is the characteristic temperature of the heated chondrules in the hot column. The optical depth τ' from $r = 0$ to $r = r'$ has two contributions from chondrules $\tau_{\rm c}'$ and dust $\tau_{\rm d}'$,

$$\tau_{\rm c}' = \int_0^{r'} \rho_{\rm c}\kappa_{\rm c} dr \tag{46}$$

and

$$\tau_{\rm d}' = \int_0^{r'} \rho_{\rm d}\kappa_{\rm d} dr, \tag{47}$$

respectively. The optical depth depends on the evolution of the density distribution. Then, the cooling rates of chondrules are approximately

$$M_{\rm c} C_{\rm sil} \left| \frac{dT_{\rm c}'}{dt} \right|_{\rm cool} \sim 2\pi r' h F'. \tag{48}$$

Below, we estimate the optical depth and cooling rates of chondrules for both decoupled and coupled cases.

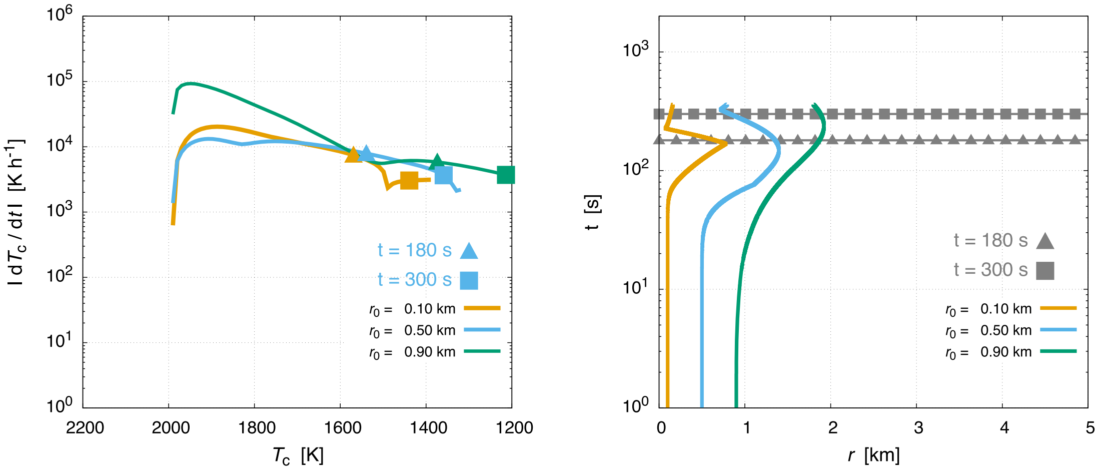

(a) run c1

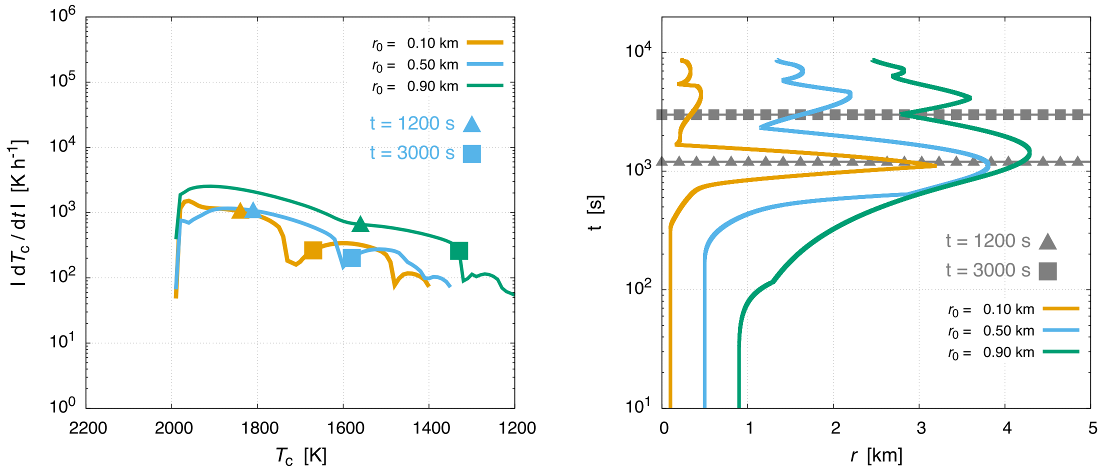

(b) run c2

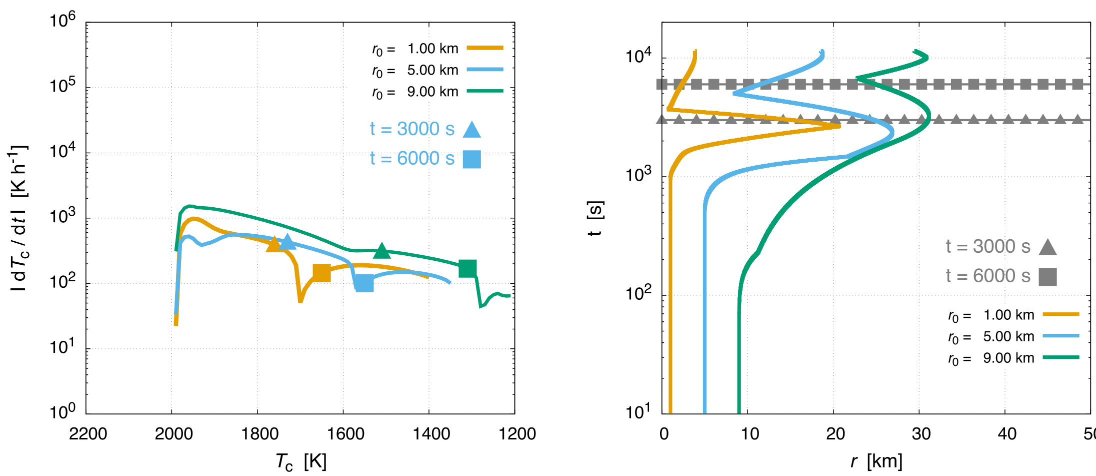

(c) run c3

Figure 11. Left: cooling rates of chondrules for runs c1 (a), c2 (b), and c3 (c). Similar to the left panels of Figure 7 but for runs c1, c2, and c3. Right: trajectories of the chondrules. The different colors of the lines indicate the different initial positions of the chondrules as in the left panels and Figure 7: $r_0 = 0.1r_{\rm dis}$ (orange), $0.5r_{\rm dis}$ (light blue), and $0.9r_{\rm dis}$ (green). Two horizontal lines indicate two different moments with the triangles and the squares on these lines.

5.2.1. Chondrule-dominated Regime in the Decoupled Case

During the expansion and return phases, the density of dusty gas around the heated chondrules considerably decreases (top panels of Figures 3 and 4), and $\tau'_{\rm c} \gg \tau'_{\rm d}$. The optical depth of the chondrules is

$$\tau'_{\rm c} = \rho_{\rm c,0}\kappa_{\rm c} r_{\rm dis} = 8.3 \times 10 \times \left(\frac{\rho_{\rm c,0}}{10^{-4}\ {\rm g\ cm^{-3}}}\right)\left(\frac{r_{\rm dis}}{1\ {\rm km}}\right)\left(\frac{a_{\rm c}}{0.3\ {\rm mm}}\right)^{-1}. \tag{49}$$

The cooling rates of chondrules are estimated to be

$$\left|\frac{dT'_{\rm c}}{dt}\right|_{\rm cool} \sim \frac{2\pi r_{\rm dis} h(\sigma_{\rm sb}T_c'^4/\tau'_{\rm c})}{M_{\rm c}C_{\rm sil}} \sim 3.2 \times 10^2\ {\rm K\ hr^{-1}}\left(\frac{\rho_{\rm c,0}}{10^{-4}\ {\rm g\ cm^{-3}}}\right)^{-2} \times \left(\frac{r_{\rm dis}}{1\ {\rm km}}\right)^{-2}\left(\frac{a_{\rm c}}{0.3\ {\rm mm}}\right)\left(\frac{T'_{\rm c}}{1600\ {\rm K}}\right)^4. \tag{50}$$

5.2.2. Pressure Balance in the Decoupled Case

In the following three regimes, we assume that dust grains are so abundant that most of their mass remains as a solid state, keeping the saturation of silicate vapor, i.e., $f_{\rm evap} \ll 1$. In other words, $\rho_{\rm d}$ in Section 5.2 is approximately equivalent to the solid dust density, while it includes the silicate vapor in the original meaning (Table 1). This assumption is valid in most of the cases.

If $p_{\rm sil}^{\rm eq} > p_{\rm H_2,0}$ in the hot region, the vapor pressure of silicate prevents dusty gas from returning to the hot region, so $\tau'_{\rm c} \gg \tau'_{\rm d}$, and the cooling rates of chondrules are the same as those of Equation (50). On the other hand, if $p_{\rm sil}^{\rm eq} < p_{\rm H_2,0}$, $\tau'_{\rm c} \ll \tau'_{\rm d}$ at pressure balance after completing the return phase. At this time, pressure balance can be described as

$$\rho'_{\rm H_2} T'_{\rm c} \simeq \rho_{\rm H_2,0} T_0 \tag{51}$$

and

$$\rho'_{\rm d} T'_{\rm c} \simeq \rho_{\rm d,0} T_0, \tag{52}$$

where $\rho'_{\rm H_2}$ and $\rho'_{\rm d}$ are the characteristic densities of hydrogen molecules and dust grains, respectively, and we replace T', the characteristic temperature of dusty gas in the hot region, with $T'_{\rm c}$ based on $T \simeq T_{\rm c}$ (bottom panels of Figures 3–5). The optical depth of the dust is

$$\tau'_{\rm d} \simeq \rho_{\rm d,0}\left(\frac{T'_{\rm c}}{T_0}\right)^{-1}\kappa_{\rm d} r_{\rm dis} = 3.1 \times 10^2\left(\frac{\rho_{\rm d,0}}{10^{-5}\ {\rm g\ cm^{-3}}}\right) \times \left(\frac{r_{\rm dis}}{1\ {\rm km}}\right)\left(\frac{a_{\rm d}}{1 \mu{\rm m}}\right)^{-1}\left(\frac{T'_{\rm c}/T_0}{1600\ {\rm K}/200\ {\rm K}}\right)^{-1}. \tag{53}$$

The cooling rates of chondrules are estimated to be

$$\left|\frac{dT'_{\rm c}}{dt}\right|_{\rm cool} \sim \frac{2\pi r_{\rm dis} h(\sigma_{\rm sb}T_c'^4/\tau'_{\rm d})}{M_{\rm c}C_{\rm sil}} \sim 8.6 \times 10^1\ {\rm K\ hr^{-1}}\left(\frac{\rho_{\rm c,0}}{10^{-4}\ {\rm g\ cm^{-3}}}\right)^{-1} \times \left(\frac{\rho_{\rm d,0}}{10^{-5}\ {\rm g\ cm^{-3}}}\right)^{-1}\left(\frac{r_{\rm dis}}{1\ {\rm km}}\right)^{-2} \times \left(\frac{a_{\rm d}}{1\ \mu{\rm m}}\right)\left(\frac{T'_{\rm c}}{1600\ {\rm K}}\right)^4\left(\frac{T'_{\rm c}/T_0}{1600\ {\rm K}/200\ {\rm K}}\right), \tag{54}$$

where the last parentheses represent the expansion of hot dusty gas. This is invalid when the vapor pressure of silicate or other species exceeds the pressure of ambient hydrogen molecules. Equations (50) and (54) validate the drop in the cooling rates due to the transition from the chondrule-dominated optical depth regime (Equation (49)) to the dust-dominated optical depth regime (Equation (53)).

5.2.3. Wall-like Structure in the Coupled Case

In the coupled case, $\tau'_{\rm c} \ll \tau'_{\rm d}$, unless the dust grains almost evaporate. When the heated materials are concentrated within the width of Δr around $r = r'$ (top panel of Figure 9(a)), the characteristic chondrule density there is

$$\rho'_{\rm c} = M_{\rm c}/2\pi r'\Delta r h = \rho_{\rm c,0}\left(\frac{2r'\Delta r}{r_{\rm dis}^2}\right)^{-1}, \tag{55}$$

and the characteristic dust density there is

$$\rho'_{\rm d} = \rho_{\rm d,0}\left(\frac{2r'\Delta r}{r_{\rm dis}^2}\right)^{-1}. \tag{56}$$

The optical depth of the dust is

$$\tau'_{\rm d} = \rho'_{\rm d}\kappa_{\rm d}\Delta r = 1.3 \times 10^3 \times \left(\frac{\rho_{\rm d,0}}{10^{-5}\ {\rm g\ cm^{-3}}}\right)\left(\frac{r_{\rm dis}}{1\ {\rm km}}\right)\left(\frac{a_{\rm d}}{1\ \mu{\rm m}}\right)^{-1}\left(\frac{r'}{r_{\rm dis}}\right)^{-1}. \tag{57}$$

The cooling rates of the chondrules are estimated to be

$$\left|\frac{dT'_{\rm c}}{dt}\right|_{\rm cool} \sim \frac{2\pi r' h(\sigma_{\rm sb}T_c'^4/\tau'_{\rm d})}{M_{\rm c}C_{\rm sil}} \sim 2.1 \times 10^2\ {\rm K\ hr^{-1}}\left(\frac{\rho_{\rm c,0}}{10^{-4}\ {\rm g\ cm^{-3}}}\right)^{-1} \times \left(\frac{\rho_{\rm d,0}}{10^{-5}\ {\rm g\ cm^{-3}}}\right)^{-1}\left(\frac{r_{\rm dis}}{1\ {\rm km}}\right)^{-2} \times \left(\frac{a_{\rm d}}{1\ \mu{\rm m}}\right)\left(\frac{T'_{\rm c}}{1600\ {\rm K}}\right)^4\left\{\frac{(r'/r_{\rm dis})^2}{10}\right\}, \tag{58}$$

where the last parentheses represent the expansion of hot dusty gas in a different way from Equation (54). A higher peak temperature or a lower ambient nebula pressure (density) leads to a stronger expansion, larger $(r'/r_{\rm dis})^2$, and faster cooling rates of chondrules.

5.2.4. Pressure Balance in the Coupled Case

Now that $\rho_{\rm c}/\rho_{\rm c,0} = \rho_{\rm d}/\rho_{\rm d,0}$ because of the complete coupling, using Equations (44) and (52),

$$\left(\frac{r'}{r_{\rm dis}}\right)^2 = \frac{T'_{\rm c}}{T_0}. \tag{59}$$

The optical depth of the dust is

$$\tau'_{\rm d} = \rho'_{\rm d}\kappa_{\rm d} r' = 2.5 \times 10^3\left(\frac{\rho_{\rm d,0}}{10^{-5}\ {\rm g\ cm^{-3}}}\right) \times \left(\frac{r_{\rm dis}}{1\ {\rm km}}\right)\left(\frac{a_{\rm d}}{1\ \mu{\rm m}}\right)^{-1}\left(\frac{T'_{\rm c}}{T_0}\right)^{-0.5}. \tag{60}$$

The cooling rates of the chondrules are estimated to be

$$\left|\frac{dT_{\rm c}'}{dt}\right|_{\rm cool} \sim \frac{2\pi r' h(\sigma_{\rm sb} T_{\rm c}'^4/\tau_{\rm d}')}{M_{\rm c} C_{\rm sil}}$$
$$\sim 8.6 \times 10^1 \ {\rm K\ hr^{-1}} \left(\frac{\rho_{\rm c,0}}{10^{-4}\ {\rm g\ cm^{-3}}}\right)^{-1} \times \left(\frac{\rho_{\rm d,0}}{10^{-5}\ {\rm g\ cm^{-3}}}\right)^{-1} \left(\frac{r_{\rm dis}}{1\ {\rm km}}\right)^{-2} \times \left(\frac{a_{\rm d}}{1\ \mu{\rm m}}\right)\left(\frac{T_{\rm c}'}{1600\ {\rm K}}\right)^4 \left(\frac{T_{\rm c}'/T_0}{1600\ {\rm K}/200\ {\rm K}}\right). \quad (61)$$

Equations (50), (54), (58), and (61) confirm that our simulations give us the results in good agreement with the analytical estimates within a factor of few. Equations (54), (58), and (61) show that the cooling rates of chondrules depend on how the hot column expands via $T_{\rm c}'/T_0$ or $(r'/r_{\rm dis})^2$.We note that the analytical estimates at the pressure balance for both decoupled and coupled cases are identical (Equations (54) and (61)).

5.3. Chondrule-forming Environments

5.3.1. Very High Solid Density

We discuss the environments that lead to extremely high solid densities inferred by Alexander et al. (2008) and considered in this paper. At the beginning, we note that these densities exceed the Roche density in the asteroid belt region. Therefore, dense regions with such high densities are likely to be gravitationally unstable and collapse into the compact bodies. During the collapse into the compact bodies, solid densities as high as $\sim 10^{-5}$–10^{-3} g cm^{-3} (Alexander et al. 2008) must be achieved. In the current theory of planet formation, gravitational collapse is a candidate mechanism for planetesimal formation (e.g., Johansen et al. 2014). So it might be possible that lightning occurs in the solid-rich environments leading to planetesimal formation via gravitational collapse.

We consider the generation of lightning in a dense clump that is gravitationally unstable. Solid particles fall into the center of the clump at the terminal velocities determined by the balance between the gravity toward the center and the drag force in the opposite direction. Larger particles fall faster than smaller ones. When different-sized particles collide, they exchange charges. Separation of these charged particles leads to the building up of electric fields and triggers lightning in the clump. However, this scenario seems to contradict the large age spreads of chondrules found in a single chondrite (e.g., Connelly et al. 2012) because the collapse ends within a much shorter period of time. If all chondrules in a single chondrite are formed in the same collapse of one clump, they must have a single age or very narrow ages. In that case, large age spreads among chondrules might be attributed to uncertainties in the measurements of chondrule ages or disturbances caused by parent body processes and do not reflect actual chondrule ages (Alexander & Ebel 2012). Alternatively, if chondrules formed in the collapse of several clumps eventually concentrate into one chondrite, it might be not so problematic. One possibility is that chondrules that are weakly bound in clumps are stripped off by surrounding sub-Keplerian gas and delivered into protoplanetary disks. Another possibility is that an older generation of planetesimals are broken or partially eroded and supply older chondrules to the formation regions of chondrite parent bodies in protoplanetary disks.

Johansen & Okuzumi (2018) suggested another scenario: circumplanetesimal disks as possible sites where rotation around the central planetesimals or protoplanets supports the gravitational stability. According to their model, solid densities at the middle of the range inferred by Alexander et al. (2008) are realized within the Hill radius of protoplanets with a radius of 1000 km in the marginally unstable circumplanetesimal disks rotating around them (see their Figure 4). Chondrules might be formed in circumplanetesimal disks via lightning triggered by the nuclear battery effect as demonstrated in Johansen & Okuzumi (2018). Chondrules located at the outermost parts of circumplanetesimal disks are stripped off from there and delivered into protoplanetary disks by headwinds from surrounding sub-Keplerian gas. These chondrules are eventually incorporated into the parent bodies of chondrites with chondrules from other parts of the same or other circumplanetesimal disks. The age spreads of chondrules might be related to the lifetimes of chondrules in circumplanetesimal disks. The viscous timescales of circumplanetesimal disks around protoplanets with a radius of 1000 km can be of the order of a few megayears depending on the random velocities of the particles (Johansen & Okuzumi 2018). Therefore, chondrule formation in circumplanetesimal disks is potentially consistent with the large age spreads of chondrules found in a single chondrite. The actual accretion timescales of circumplanetesimal disks and lifetimes of chondrules are likely to be regulated by the rates of solid supply into circumplanetesimal disks from surrounding protoplanetary disks. So we need further understanding of the interaction between circumplanetesimal disks and protoplanetary disks.

5.3.2. Even Consistent with Lightning?

For the operation of lightning, the number density of electrons must exponentially increase due to the ionizing neutral–electron collisions. However, if small dust grains are very abundant, as considered in this paper, electrons hitting the small dust grains would be absorbed by these grains, and the number density of electrons might no longer increase. The requisite condition for the operation of lightning is that electrons must collide with neutrals more frequently than small dust grains. In other words, the mean free path of the neutral–electron collisions $\lambda_{\rm ne}$ (Equation (1)) must be smaller than that of the dust–electron collisions $\lambda_{\rm de}$. The dust–electron mean free path is

$$\lambda_{\rm de} = 40\ {\rm cm}\left(\frac{\rho_{\rm d}}{10^{-5}\ {\rm g\ cm^{-3}}}\right)^{-1}\left(\frac{a_{\rm d}}{1\ \mu{\rm m}}\right), \quad (62)$$

and the ratio between $\lambda_{\rm de}$ and $\lambda_{\rm ne}$ is

$$\frac{\lambda_{\rm de}}{\lambda_{\rm ne}} = 5.6 \times 10^{-1}\left(\frac{\rho_{\rm d}}{10^{-5}\ {\rm g\ cm^{-3}}}\right)^{-1} \times \left(\frac{\rho_{\rm H_2}}{10^{-10}\ {\rm g\ cm^{-3}}}\right)\left(\frac{a_{\rm d}}{1 \mu{\rm m}}\right), \quad (63)$$

where Equation (63) must be larger than unity for the operation of lightning.

Substituting the ratio $\lambda_{\rm de}/\lambda_{\rm ne}$ (Equation (63)) and the scaling factor $f_{\rm dis}$ (Equation (2)) into the cooling rates of chondrules at the pressure balance (Equations (54) and (61)) yields

$$\left|\frac{dT_c'}{dt}\right|_{\rm cool} \sim 3.0 \times 10^2\ {\rm K\ hr^{-1}} \left(\frac{\lambda_{\rm de}}{\lambda_{\rm ne}}\right) \times \left(\frac{\rho_c}{10^{-4}\ {\rm g\ cm^{-3}}}\right)^{-1} \left(\frac{\rho_{\rm H_2}}{10^{-10}\ {\rm g\ cm^{-3}}}\right) \left(\frac{f_{\rm dis}}{10^3}\right)^{-2} \times \left(\frac{T_c'}{1600\ {\rm K}}\right)^4 \left(\frac{T_c'/T_0}{1600\ {\rm K}/200\ {\rm K}}\right). \tag{64}$$

Even if $\lambda_{\rm de}/\lambda_{\rm ne} = 10$, lightning discharge with a radius of $3 \times 10^3 < f_{\rm dis} < 10^4$ satisfies the desired cooling rates of $\sim 10^1$–$10^3\ {\rm K\ hr^{-1}}$.

5.3.3. Presence and Role of Small Dust Grains

The presence of small dust grains is essential to the cooling rates of chondrules. In the decoupled case, although the analytical estimate of the cooling rates of chondrules in the chondrule-dominated optical depth regime (Equation (50)) is within the proper range of $\sim 10^1$–$10^3\ {\rm K\ hr^{-1}}$ for our fiducial parameters, Figure 7(b) shows that numerical results are close to or slightly above the upper limit of this range, especially for chondrules located at the outer edge of discharge channel ($r_0 = 0.9$ km). Only after the sudden drop (Figure 7(b)) due to the return of dusty gas into the hot region can the cooling rates of chondrules match the proper range of cooling rates, even if we consider the middle solid density inferred by Alexander et al. (2008) for chondrule density. In the coupled case, the cooling rates of chondrules without the contribution from small dust grains are 30 ($= \rho_d \kappa_d / \rho_c \kappa_c$) times faster than those including small dust grains. Even at the pressure balance, the cooling rates of chondrules are above the range of $\sim 10^1$–$10^3\ {\rm K\ hr^{-1}}$, although not far beyond.

Given the roles of small dust grains in the cooling rates of chondrules, we need to consider how such a high abundance of small dust grains as that of chondrules is supplied to chondrule-forming environments. Particle concentration mechanisms in protoplanetary disks (e.g., Cuzzi et al. 2001; Youdin & Goodman 2005), which might be followed by gravitational collapse to form planetesimals, are size-dependent phenomena, and the accretion of particles onto circumplanetesimal disks is likely to be as well. Small dust grains are strongly coupled to the dynamics of gas and might not concentrate in clumps or accrete onto circumplanetesimal disks.

However, small dust grains are expected to be generated via collisional fragmentation of large particles such as chondrule precursors. In an often-used simple model for the size distribution of particles in coagulation and fragmentation equilibrium (e.g., Drazkowska et al. 2016), the number density of particles as a function of their sizes is approximated as $n(a) \propto a^{-3.5}$, where n is the number density per unit size, and a is the particle's size. In this power-law size distribution, the mass density ($\propto \rho_{\rm mat} a^3 n(a) \times a$) ratio between small dust grains ($\sim 1\ \mu$m) and chondrules (~ 0.3 mm) is $\sim (1\ \mu{\rm m}/0.3\ {\rm mm})^{0.5} \sim 0.058$, and the total mass of small dust grains is roughly a few percent to one-tenth of that of chondrules. Moreover, small dust grains dominate the surface area ($\propto a^2 n(a) \times a$) and contribute to the larger fraction of the total optical depth of discharge channels compared to chondrules.

Recondensation of vapor evaporated from chondrules and their precursors might also generate small dust grains to some degree. While we do not treat evaporation from chondrules for simplicity in our calculations, we evaluate the amount of vapor potentially evaporated from chondrules to discuss both the generation of small dust grains and the survivability of chondrules against evaporation in Section 5.4.

5.3.4. Compound Chondrule Frequency

A few percent of the chondrules are apparently fused together making compounds (e.g., Wasson et al. 1995). From this observation, one can infer that the average number of mergers one chondrule experienced during the molten phase, $N_{\rm merge}$, was around 0.01–0.05. The number $N_{\rm merge}$ can be equated as follows:

$$N_{\rm merge} = 4\pi a_c^2 n_c f_{\rm stick} \Delta v \Delta t = 1.2 \times 10^3 f_{\rm stick} \left(\frac{\rho_c}{10^{-4}\ {\rm g\ cm^{-3}}}\right) \times \left(\frac{a_c}{0.3\ {\rm mm}}\right)^{-1} \left(\frac{\Delta v}{1\ {\rm m\ s^{-1}}}\right) \left(\frac{\Delta t}{1\ {\rm hr}}\right), \tag{65}$$

where $f_{\rm stick}$ is the sticking probability after a collision, Δv is the relative velocity between chondrules, and Δt is the time interval for compound formation. We use our fiducial chondrule density for the normalization, and such an extremely high density easily leads to a number of mergers many orders of magnitude higher than the observation. In principle, Δv is uncertain from our calculations because we simplify the dynamics of chondrules. However, we can still have a rough consideration regarding Δv. According to our calculation for run c2, chondrules, dynamically coupled with surrounding dusty gas, move at $v \sim 10^{-3}$–$10^{-2}\ {\rm km\ s^{-1}}$ (Figure 9). If we assume tentative $\sim 10\%$ variations in the velocities between chondrules, depending on their aerodynamic properties, the relative velocity between chondrules is $\Delta v \sim 0.1 v \sim 0.1$–$1\ {\rm m\ s^{-1}}$. In the decoupled run d2, although the velocity of the surrounding dusty gas reaches as fast as $v \sim 1\ {\rm km\ s^{-1}}$ (Figure 3), chondrules experience little drag from fast gas and dust. Therefore, the velocity difference Δv between chondrules is orders of magnitude lower than the velocity v of the dusty gas. Anyway, even assuming a difference Δv of $\sim 1\ {\rm m\ s^{-1}}$ or less, it seems that our model with the high chondrule density is incompatible with the actual compound chondrule frequency found in meteorites. However, this problem can be mitigated from some perspectives.

The sticking probability $f_{\rm stick}$ must be smaller than unity as a function of the collisional conditions (e.g., impact velocity, impact parameter, and size ratio) and the material properties of chondrule melts (e.g., viscosity and surface energy). The viscosity of chondrule melts sensitively depends on the temperature, and it decreases with increasing temperature (Arakawa & Nakamoto 2019; Jacquet 2021). On the other hand, the surface energy of the melts is almost constant during cooling (Arakawa & Nakamoto 2019; Jacquet 2021). Consequently, qualitatively speaking, the collisional outcomes behave as the inviscid limit at high temperature due to relatively low viscosity. The critical velocity for sticking between two inviscid droplets is well described using the

Weber number We,

$$\mathrm{We} \equiv \frac{2\rho_{\mathrm{mat}} a_{\mathrm{c}} \Delta v^2}{\sigma}, \tag{66}$$

where σ is the surface energy of chondrule melts, and we adopt $400\,\mathrm{erg\,cm^{-2}}$ (Arakawa & Nakamoto 2019). We assume that the melt density is equivalent to the material density of silicate particles. While the critical Weber number $\mathrm{We}_{\mathrm{crit}}$ for sticking depends on the impact parameter and size ratio, $\mathrm{We}_{\mathrm{crit}} \sim 10^1$–$10^2$ for nearly the same-sized droplets (Ashgriz & Poo 1990). The critical velocity for sticking at the inviscid limit is

$$\Delta v_{\mathrm{crit}} \sim 1.5\ \mathrm{m\ s^{-1}} \left(\frac{\mathrm{We}_{\mathrm{crit}}}{10}\right)^{0.5} \left(\frac{a_{\mathrm{c}}}{0.3\ \mathrm{mm}}\right)^{-0.5}. \tag{67}$$

During the periods of the inviscid melts at high temperatures, the collisions at the velocities of $\Delta v \gg 1\,\mathrm{m\,s^{-1}}$ lead to the separation or shattering of droplets, and f_{stick} is very low. Therefore, $f_{\mathrm{stick}}\Delta v$ might be below $1\,\mathrm{m\,s^{-1}}$.

Even if the colliding pairs of droplets stick with each other, the resultant compounds quickly deform into spherules and cannot be recognized as compound chondrules due to relatively high surface tension and low viscosity of chondrule melts. Jacquet (2021) estimated that the deformation timescale is less than the cooling timescale (more strictly, the e-folding time of the change in the deformation timescale due to cooling) at a temperature above 1220, 1280, and 1360 K for cooling rates of 10, 10^2, and $10^3\,\mathrm{K\,hr^{-1}}$, respectively, which are below or close to our modeled solidus temperature $T_{\mathrm{solid}} = 1400$ K. Therefore, the formation of recognizable compound chondrules might only be limited to around the glass transition temperature of mesostases (Alexander & Ebel 2012). If the temperature interval of their formation is $\sim$100 K and the cooling rates of chondrules are $\sim 10^3\,\mathrm{K\,hr^{-1}}$, the time interval of the formation is $\Delta t \sim 0.1$ hr, and N_{merge} decreases by 1 order of magnitude from the value shown in Equation (65).

Furthermore, most of chondrules are nonspherical (e.g., 60%–75% of chondrules in CO3 chondrites; Rubin & Wasson 2005) and might have originated from the mergers of two or more droplets (Alexander & Ebel 2012; Jacquet 2021). In this case, nonspherical chondrules represent a small fraction of the mergers because most compounds quickly turn into perfect spherules due to surface tension (Alexander & Ebel 2012). The actual number of mergers N_{merge}, therefore, can be more than unity.

In conclusion, we consider that the following condition for chondrule formation is compatible with the operation of lightning, the desired cooling rates reported from the experiments, and the observations of compound and nonspherical chondrules. Here we regard N_{merge} as the number of mergers that creates recognizable compounds and nonspherical chondrules instead of the total number of mergers during the whole cooling. The lower limit of the solid density deduced by Alexander et al. (2008; $\sim 10^{-5}\,\mathrm{g\,cm^{-3}}$) for chondrule density ρ_{c}, scaling factor of channel radius $f_{\mathrm{dis}} \sim 3\times10^3$, and $\lambda_{\mathrm{de}}/\lambda_{\mathrm{ne}}$ of a factor of a few leads to cooling rates of $10^3\,\mathrm{K\,hr^{-1}}$ (Equation (64)), which is the upper limit from the experiments. At this condition, the dust density is $\rho_{\mathrm{d}} \sim 10^{-6}\,\mathrm{g\,cm^{-3}}$ (Equation (63)) and 1 order of magnitude lower than that of chondrules. The temperature interval for the formation of recognizable compounds and nonspherical chondrules is limited to $\sim$100 K, and the corresponding time interval is $\Delta t \sim 0.1$ hr. Combined with $f_{\mathrm{stick}} \sim 1$ and $\Delta v \sim 1\,\mathrm{m\,s^{-1}}$, $N_{\mathrm{merge}} \sim 10$. The sticking probability and relative velocity between chondrules are the most uncertain parameters. Actually, near the glass transition temperature, the viscosity of melts is so high that collisional outcomes no longer follow the inviscid behavior, and $f_{\mathrm{stick}}\Delta v$ can be much larger than $1\,\mathrm{m\,s^{-1}}$. We need more thorough studies of these parameters in a future work. Finally, we note that many mergers between chondrule precursors erase the compositional diversity of precursors. Hezel & Palme (2007) estimated that the number of mergers between heterogeneous precursors must be less than 10 to preserve their heterogeneity. In the above consideration, $N_{\mathrm{merge}} \sim 10$ means that the total number of mergers during the whole cooling is more than 10 (likely $\sim$100), which seems to contradict the chemical diversity of chondrules. One possibility is that the chemical diversity of chondrules originates from chemical heterogeneity between subregions within a single chondrule-forming region, and chondrules formed in various subregions begin to be mixed at the time of formation of recognizable compounds and nonspherical chondrules (Alexander & Ebel 2012). Another possibility is that $f_{\mathrm{stick}}\Delta v < 1\,\mathrm{m\,s^{-1}}$, and $N_{\mathrm{merge}} < 10$.

5.4. Survivability of Chondrules against Evaporation

According to the Hertz–Knudsen equation, the net evaporation flux of forsterite is given as follows:

$$j_{\mathrm{Fo}} = \frac{\alpha_{\mathrm{SiO}}(P_{\mathrm{SiO}}^{\mathrm{eq}} - P_{\mathrm{SiO}})}{\sqrt{2\pi m_{\mathrm{SiO}} k_{\mathrm{B}} T}}, \tag{68}$$

where j_{Fo} is the number of forsterite molecules evaporated from unit surface area in unit time, α_{SiO} is the evaporation coefficient of SiO, $P_{\mathrm{SiO}}^{\mathrm{eq}}$ and P_{SiO} are the equilibrium and ambient pressure of SiO, and m_{SiO} is the molecular mass of SiO. Assuming congruent evaporation under chemical reaction (35), $P_{\mathrm{sil}}^{\mathrm{eq}} = P_{\mathrm{Mg}}^{\mathrm{eq}} + P_{\mathrm{SiO}}^{\mathrm{eq}} + P_{\mathrm{O_2}}^{\mathrm{eq}} = 4.5P_{\mathrm{SiO}}^{\mathrm{eq}}$ (Equation (36); see also Miura et al. 2002). In a vacuum, the evaporation mass flux of forsterite is

$$J_{\mathrm{Fo}} = m_{\mathrm{Fo}} j_{\mathrm{Fo}} = \frac{\alpha_{\mathrm{SiO}} m_{\mathrm{Fo}} P_{\mathrm{sil}}^{\mathrm{eq}}/4.5}{\sqrt{2\pi m_{\mathrm{SiO}} k_{\mathrm{B}} T}}, \tag{69}$$

where m_{Fo} is the molecular mass of forsterite (not $\bar{m}_{\mathrm{Fo}}$ in Equation (34), which is the average mass of vapor species Mg, SiO, and $\mathrm{O_2}$). The evaporation coefficient is less than unity and about 0.1 in wide temperature and pressure ranges (e.g., Tsuchiyama et al. 1999). So we adopt $\alpha_{\mathrm{SiO}} = 0.1$ for simplicity here. The evaporation timescale of silicate particles in a vacuum is

$$t_{\mathrm{evap}} = \frac{a\rho_{\mathrm{mat}}}{J_{\mathrm{Fo}}}. \tag{70}$$

Chondrules ($a = 300\,\mu$m) evaporate within $t_{\mathrm{evap}} = 0.27$, 4.3, 130, and 8800 hr at temperatures of 2200, 2000, 1800, and 1600 K, respectively. Even during cooling from 2200 to 2000 K, it takes more than 0.27 hr for chondrules to vanish via evaporation. Cooling rates at this temperature range are faster than $10^3\,\mathrm{K\,hr^{-1}}$ for the runs that show the desired cooling rates of 10^1–$10^3\,\mathrm{K\,hr^{-1}}$ during crystallization (Figures 7, 8, and 11). Cooling timescales from 2200 to 2000 K are less than 0.2 hr.

Therefore, chondrules can survive evaporation. However, some fractions of chondrule mass might evaporate and be converted into small dust grains via condensation if the chondrule temperature reaches as high as 2200 K.

5.5. More Volatile Species than Forsterite

In this study, the evaporation of the most refractory silicate, forsterite, is implemented into the simulations. However, more volatile species must have existed in the chondrule-forming events. In particular, we did not consider the contributions from water vapor assuming chondrule-forming events of ordinary chondrites inside the water snowline. Here we discuss chondrule formation of carbonaceous chondrites via lightning outside the water snowline.

5.5.1. Water Vapor in Chondrule-forming Environments

The measurements of the Mg/Fe and oxygen isotope ratios of the constituent minerals (olivine and pyroxene) in chondrules from carbonaceous chondrites reveal the correlation between the oxygen fugacities and the oxygen isotope compositions in chondrule-forming environments (e.g., Connolly & Huss 2010; Ushikubo et al. 2012; Tenner et al. 2015; Hertwig et al. 2018). Moreover, chondrules from primitive carbonaceous chondrites plot along the line with the slope of almost unity in the three oxygen isotope diagram (e.g., Ushikubo et al. 2012; Tenner et al. 2015; Hertwig et al. 2018). This trend contrasts with the terrestrial fractionation line with a slope of 0.52 and likely reflects the mass-independent process (e.g., Yurimoto & Kuramoto 2004; Lyons & Young 2005). These facts indicate a reservoir of an oxidizing agent with the heavier oxygen isotope composition (e.g., Connolly & Huss 2010; Ushikubo et al. 2012; Tenner et al. 2015; Hertwig et al. 2018). Water is an ubiquitous species in protoplanetary disks and might have been such an oxidizing agent in the solar nebula (e.g., Connolly & Huss 2010; Ushikubo et al. 2012). Therefore, it is important to consider the effects of water on the evolution during chondrule-forming events for each candidate model from both the chemical and physical perspectives.

5.5.2. Influence on the Cooling Rates of Chondrules

In the lightning model, water vapor increases the total pressure in the hot column. The estimates of the cooling rates at the pressure balance in Equations (54) and (61) assume that the partial pressure of vapor species evaporated from the solid particles is negligible compared to the pressure of hydrogen molecules. However, if a substantial amount of water vapor exists in the hot column, a much stronger expansion of the hot column occurs, and the return phase does not complete before chondrules solidify from melts. This results in faster cooling rates of chondrules, and the lightning model might fail to reproduce the proper cooling rates of chondrules reported from the experiments even if we assume the extremely high solid density in the literature (Alexander et al. 2008).

5.5.3. Suspension of the Discharge Currents

We consider that there is another potential problem regarding the existence of the volatile species. We set the hot column with the peak temperature as the initial state and do not consider the initial energy release from the electric field via the discharge currents. It is equivalent to the approximation that the duration of the discharge is infinitely short compared to the dynamic time of dusty gas and the succeeding cooling phase. However, it can take a finite time for the discharging currents to release enough energy to melt chondrules. In such a case, the initial gas with hydrogen molecules might be contaminated with the vapor evaporated from the solid particles. It leads to the decrease in the mean free path of electrons and weaker acceleration of electrons from the electric field before the collisions with the neutrals. It might result in suspending the ionization cascade and the discharge process. To judge whether the contamination with the evaporated vapor ceases the discharge currents or not, we need a further understanding of the detailed physics of the discharge process.

5.6. Caveats and Future Work

5.6.1. Evaporation from Chondrules

We did not consider the evaporation from chondrules because it complicates the calculations. However, we need to consider the evaporation of silicate and the other species from both dust grains and chondrules to confirm that chondrules really can retain volatile species such as sodium in the lightning model. It is important because the retention of volatiles is the direct motivation to assume the extremely high solid density in the chondrule-forming environments (Alexander et al. 2008). More sophisticated treatments of the coupling of chondrules with dusty gas via the drag force and the evaporation and condensation equations are also required for this issue. In the decoupled case, the density of dusty gas around the chondrules in the hot region significantly decreases, and the vapor expanding outward recondenses in the cold outer region. Volatiles evaporated from hot chondrules might follow the same evolutionary sequence and might not recondense onto the parent chondrules. Such volatiles would be lost from hot chondrules. However, it does not necessarily mean that chondrules fail to retain volatiles. The key points are the evaporation rates from chondrules and the duration of the expanding phase. If the evaporation of volatiles from chondrules is slow enough, the chondrules would preserve these species. On the other hand, in the coupled case, chondrules can retain volatiles after their solidification unless the volatiles recondense onto the small dust grains because volatiles do not escape from the parcel of dusty gas and chondrules.

5.6.2. Diffusion

In our model, we solve the hydrodynamics equations without the molecular diffusion. It might be a good approximation for the problems with scales much larger than the mean free path of the molecules. However, the width of the discharge channel is not large enough to apply this approximation without any concerns. The molecular diffusion might be another thread for chondrules to retain the volatile species and makes the cooling rates of chondrules faster by the escape of the heat. Cuzzi & Alexander (2006) estimated that the length scale of chondrule-forming events must be larger than 150–6000 km to suppress isotopic fractionation of volatiles. The width of the lightning discharge is likely to be less than 150–6000 km in the asteroid region. However, the density of chondrules in this paper and expected in Alexander et al. (2008) is much larger than the minimum density required to reach the saturation of the vapor in Cuzzi & Alexander (2006), and the length scale of chondrule-forming events can be smaller than 150–6000 km.

6. Conclusion

In this study, we revisit the cooling rates of chondrules predicted by the lightning model in solid-rich environments. Previous works considered that the discharge channels are optically thin, and the cooling rates of chondrules are those of the isolated chondrules in space (e.g., Horányi et al. 1995; Desch et al. 2012). However, the buildup of the electric fields in the protoplanetary disks requires efficient charging and charge separation mechanisms with high solid enhancement to overcome the neutralizing currents (e.g., Desch & Cuzzi 2000; Muranushi 2010; Johansen & Okuzumi 2018). Moreover, the properties of chondrules indicate their formation in such environments (e.g., Cuzzi & Alexander 2006; Alexander et al. 2008). It is more straightforward that the discharge channels are optically thick, and the cooling rates of chondrules are much slower than those of the isolated chondrules due to the absorption of the radiation from the neighborhood chondrules.

Our calculations include hydrodynamic expansion, radiative transfer, thermal collision between chondrules and gas-phase species, and evaporation of the small dust grains. Chondrules must dynamically interact with their surrounding dusty gas. We consider the two limiting cases for chondrule dynamics: the decoupled case and the coupled case. The drag force is ignored, and chondrules stay at their initial positions in the decoupled case. On the other hand, chondrules move with dusty gas in the coupled case.

Our findings are summarized as follows.

1. In both the decoupled and coupled cases, there are three phases of evolution: the initial expansion phase, the intermediate return phase, and the final pressure balance phase.
2. In the decoupled case, the density of dusty gas significantly decreases in the hot region during the expansion phase if we include the evaporation of the dust grains. The cooling rates of chondrules suddenly drop after the return phase because the optical depth of the hot region becomes larger due to the transition from the chondrule-dominated optical depth regime to the dust-dominated optical depth regime. If chondrules solidify from melts faster than the completion of the return phase, there is no drop in the cooling rates of chondrules during their crystallization.
3. In the coupled case, hot chondrules are concentrated in the inner edge of the wall-like structure during the expansion phase if we include the evaporation of the dust grains. The cooling rates of chondrules oscillate due to the oscillation of the trajectories of chondrules.
4. In both the decoupled and coupled cases, the reasonable radius of the discharge channel in the solar nebula (e.g., Horányi et al. 1995) and the solid density expected from the retention of sodium in chondrules (e.g., Alexander et al. 2008) lead to the proper cooling rates of chondrules within the range of 10^1–10^3 K hr^{-1} (Desch et al. 2012, and references therein).
5. The expanding materials cannot return to the inner region unless the partial pressures of the evaporated species become weaker than the ambient pressure of nebula hydrogen molecules. If a substantial amount of the vapor of the volatile species exists in the chondrule-forming environments, the expansion must be stronger than shown in this paper, and the cooling rates of chondrules must be faster than estimated in this paper. It points out the importance of the vapor pressure of volatile species such as water, which is ubiquitous in the protoplanetary disks and might have existed in the forming regions of chondrules in carbonaceous chondrites to various degrees (e.g., Connolly & Huss 2010; Ushikubo et al. 2012; Tenner et al. 2015; Hertwig et al. 2018).

We are grateful to the anonymous reviewers for their fruitful comments. H.K. is supported by JST SPRING grant No. JPMJSP2106. T.N. is supported by JSPS KAKENHI grant Nos. JP18K03721 and JP22K03698.

ORCID iDs

Hiroaki Kaneko https://orcid.org/0000-0002-1481-6313
Taishi Nakamoto https://orcid.org/0000-0003-3924-6174

References

Alexander, C. M. O., & Ebel, D. S. 2012, M&PS, 47, 1157
Alexander, C. M. O., Grossman, J. N., Ebel, D. S., & Ciesla, F. J. 2008, Sci, 320, 1617
Arakawa, S., & Nakamoto, T. 2019, ApJ, 877, 84
Ashgriz, N., & Poo, J. Y. 1990, JFM, 221, 183
Asphaug, E., Jutzi, M., & Movshovitz, N. 2011, E&PSL, 308, 369
Boley, A. C., Morris, M. A., & Desch, S. J. 2013, ApJ, 776, 101
Boss, A. P., & Durisen, R. H. 2005, ApJL, 621, L137
Choksi, N., Chiang, E., Connolly, H. C., Jr., Gainsforth, Z., & Westphal, A. J. 2021, MNRAS, 503, 3297
Ciesla, F. J., & Hood, L. L. 2002, Icar, 158, 281
Ciesla, F. J., Hood, L. L., & Weidenschilling, S. J. 2004, M&PS, 39, 1809
Connelly, J. N., Bizzarro, M., Krot, A. N., et al. 2012, Sci, 338, 651
Connolly, H. C., & Jones, R. H. 2016, JGRE, 121, 1885
Connolly, H. C., Jr., & Huss, G. R. 2010, GeCoA, 74, 2473
Cuzzi, J. N., & Alexander, C. M. O. 2006, Natur, 441, 483
Cuzzi, J. N., Hogan, R. C., Paque, J. M., & Dobrovolskis, A. R. 2001, ApJ, 546, 496
Desch, S. J., & Connolly, H. C. 2002, M&PS, 37, 183
Desch, S. J., & Cuzzi, J. N. 2000, Icar, 143, 87
Desch, S. J., Morris, M. A., Connolly, H. C., Jr., & Boss, A. P. 2012, M&PS, 47, 1139
Drazkowska, J., Alibert, Y., & Moore, B. 2016, A&A, 594, A105
Dullemond, C. P., Harsono, D., Stammler, S. M., & Johansen, A. 2016, ApJ, 832, 91
Dullemond, C. P., Stammler, S. M., & Johansen, A. 2014, ApJ, 794, 91
Ebert, U., Nijdam, S., Li, C., et al. 2010, JGRA, 115, A00E43
Eisenhour, D. D., Daulton, T. L., & Buseck, P. R. 1994, Sci, 265, 1067
Hasegawa, Y., Wakita, S., Matsumoto, Y., & Oshino, S. 2016, ApJ, 816, 8
Hayashi, C. 1981, PThPS, 70, 35
Hertwig, A. T., Defouilloy, C., & Kita, N. T. 2018, GeCoA, 224, 116
Hezel, D. C., & Palme, H. 2007, GeCoA, 71, 4092
Hood, L. L. 1998, M&PS, 33, 97
Hood, L. L., & Horanyi, M. 1991, Icar, 93, 259
Horányi, M., Morfill, G., Goertz, C. K., & Levy, E. H. 1995, Icar, 114, 174
Iida, A., Nakamoto, T., Susa, H., & Nakagawa, Y. 2001, Icar, 153, 430
Jacquet, E. 2021, GeCoA, 296, 18
Jacquet, E., & Thompson, C. 2014, ApJ, 797, 30
Johansen, A., Blum, J., Tanaka, H., et al. 2014, Protostars and Planets VI (Tucson, AZ: Univ. Arizona Press), 547
Johansen, A., & Okuzumi, S. 2018, A&A, 609, A31
Johnson, B. C., Minton, D. A., Melosh, H. J., & Zuber, M. T. 2015, Natur, 517, 339
Lichtenberg, T., Golabek, G. J., Dullemond, C. P., et al. 2018, Icar, 302, 27
Lyons, J. R., & Young, E. D. 2005, Natur, 435, 317
Mai, C., Desch, S. J., Boley, A. C., & Weiss, B. P. 2018, ApJ, 857, 96
Mann, C. R., Boley, A. C., & Morris, M. A. 2016, ApJ, 818, 103
Miura, H., Nakamoto, T., & Susa, H. 2002, Icar, 160, 258

Morris, M. A., Boley, A. C., Desch, S. J., & Athanassiadou, T. 2012, ApJ, 752, 27
Muranushi, T. 2010, MNRAS, 401, 2641
Nagasawa, M., Tanaka, K. K., Tanaka, H., et al. 2019, ApJ, 871, 110
Nakamura, T., Noguchi, T., Tsuchiyama, A., et al. 2008, Sci, 321, 1664
Rubin, A. E., & Wasson, J. T. 2005, GeCoA, 69, 211
Scott, E. R. D., & Krot, A. N. 2014, in Meteorites and Cosmochemical Processes, ed. A. M. Davis (Amsterdam: Elsevier), 65
Stone, J. M., Mihalas, D., & Norman, M. L. 1992, ApJS, 80, 819
Stone, J. M., & Norman, M. L. 1992, ApJS, 80, 753
Tenner, T. J., Nakashima, D., Ushikubo, T., Kita, N. T., & Weisberg, M. K. 2015, GeCoA, 148, 228
Tsuchiyama, A., Tachibana, S., & Takahashi, T. 1999, GeCoA, 63, 2451
Ushikubo, T., Kimura, M., Kita, N. T., & Valley, J. W. 2012, GeCoA, 90, 242
Wakita, S., Johnson, B. C., Denton, C. A., & Davison, T. M. 2021, Icar, 360, 114365
Wakita, S., Matsumoto, Y., Oshino, S., & Hasegawa, Y. 2017, ApJ, 834, 125
Wasson, J. T., Krot, A. N., Lee, M. S., & Rubin, A. E. 1995, GeCoA, 59, 1847
Weidenschilling, S. J., Marzari, F., & Hood, L. L. 1998, Sci, 279, 681
Wood, J. A. 1996, M&PS, 31, 641
Youdin, A. N., & Goodman, J. 2005, ApJ, 620, 459
Yurimoto, H., & Kuramoto, K. 2004, Sci, 305, 1763